

## LARGE ANGULAR SCALE POLARIZATION OF THE COSMIC MICROWAVE BACKGROUND RADIATION AND THE FEASIBILITY OF ITS DETECTION

BRIAN KEATING,<sup>1,2,3</sup> PETER TIMBIE,<sup>1,4</sup> ALEXANDER POLNAREV,<sup>5</sup> AND JULIA STEINBERGER<sup>2</sup>

Received 1997 April 21; accepted 1997 October 16

### ABSTRACT

In addition to its spectrum and temperature anisotropy, the 2.7 K cosmic microwave background (CMB) is also expected to exhibit a low level of polarization. The spatial power spectrum of the polarization can provide details about the formation of structure in the universe as well as its ionization history. Here we calculate the magnitude of the CMB polarization in various cosmological scenarios, with both an analytic and a numerical method. We then outline the fundamental challenges to measuring these signals and focus on two of them: achieving adequate sensitivity and removing contamination due to foreground sources. We describe the design of a ground-based instrument (Polarization Observations of Large Angular Regions) that could detect polarization of the CMB at large angular scales in the next few years.

*Subject headings:* cosmic microwave background — cosmology: theory — polarization

### 1. INTRODUCTION

The 2.7 K cosmic microwave background (CMB) radiation is a vital probe of all modern cosmological theories. This radiation provides a “snapshot” of the epoch at which radiation and matter decoupled approximately 300,000 years after the big bang and carries the imprint of the ionization history of the universe. This information tightly constrains theories of cosmological structure formation.

The three defining characteristics of this radiation are its spectrum, spatial anisotropy, and polarization. The spectrum and anisotropy of the CMB have both been extensively studied. The *COBE* Far-Infrared Absolute Spectrophotometer (FIRAS) has determined the blackbody temperature of the CMB to be  $2.728 \pm 0.004$  K (Fixsen et al. 1996), and the *COBE* Differential Microwave Radiometer (DMR) experiment has detected spatial anisotropy of the CMB on  $10^\circ$  scales of  $\Delta T/T \simeq 1.1 \times 10^{-5}$  (Bennett et al. 1996). Ground- and balloon-based experiments have also detected anisotropy at smaller scales; see Scott, Silk, & White (1995) for a review of these results. However, the polarization of the CMB has received comparatively little experimental attention despite its fundamental nature. The anisotropy and polarization depend in different ways on the power spectrum of fluctuations as well as on the ionization history of the universe. A detection of polarization would complement the detections of anisotropy by facilitating the reconstruction of the initial spectrum of perturbations as well as the ionization history of the universe.

The magnitude and spatial distribution of polarization is determined by factors such as the source of the CMB anisotropy, the density parameter  $\Omega$ , the baryon content of the universe  $\Omega_B$ , the Hubble constant  $H$ , and the ionization history of the universe. CMB polarization is uniquely sensitive to the ionization history of the universe, which includes

the duration of recombination and the epoch of reionization. The detection of, or a further constraint on, the polarization of the CMB has the potential to dramatically enhance our understanding of the pregalactic evolution of the universe.

Like the CMB anisotropy power spectrum, the polarization power spectrum contains information on all angular scales. Large angular scales (larger than  $\simeq 1^\circ$ ) correspond to regions on the last scattering surface that were larger than the causal horizon. In the absence of reionization, these scales were affected only by the long-wavelength modes of the primordial power spectrum. This region of the power spectrum was measured by the *COBE* DMR and establishes the normalization for models of large scale structure formation. Similarly, measurements of polarization at large angular scales will normalize the entire polarization power spectrum. Because the anticipated signal size is small at all angular scales, polarization measurements pose a significant challenge. While signals from large angular scales may be weaker than at small scales, the design of a large angular scale measurement is comparatively simple and compact, with potentially lower susceptibility to sources of systematic error. A detection or improved upper limit at large angular scales is a natural first step toward probing the polarization power spectrum on all angular scales.

In this paper, we review theoretical arguments that suggest that the ratio of polarization to anisotropy should be in the range 0.1% to 10% at large angular scales. Existing upper limits on polarization are higher than or comparable to the measured anisotropy level itself (see Table 1). Measurements of anisotropy by *COBE* and other experiments on the level of  $\Delta T/T_{\text{CMB}} \simeq 1 \times 10^{-5}$  indicate that the required level of sensitivity to polarization must be at least  $\Delta T/T_{\text{CMB}} \leq 1 \times 10^{-6}$ . Thus, to obtain new nontrivial information, either a positive detection or an improved upper limit capable of discriminating between different cosmological scenarios, requires extremely precise measurements.

Current detector technology is capable of achieving the required level of sensitivity. However, in addition to achieving high sensitivity, it is essential to discriminate the polarization from systematic effects, such as noncosmological astrophysical sources of polarized radiation. Space-based missions such as the *Microwave Anisotropy Probe* (*MAP*)

<sup>1</sup> Department of Physics, University of Wisconsin at Madison, 1150 University Avenue, Madison, WI 53706.

<sup>2</sup> Department of Physics, Brown University, Box 1843 Providence, RI 02912.

<sup>3</sup> keating@wisp5.physics.wisc.edu.

<sup>4</sup> timbie@wisp5.physics.wisc.edu.

<sup>5</sup> Astronomy Unit, Queen Mary and Westfield College, Mile End Road, London UK E14NS.

TABLE 1  
EXPERIMENTAL LIMITS ON LINEAR POLARIZATION (95% CONFIDENCE LEVEL)

Reference	Frequency (GHz)	Sky Coverage	Limit $T_{\text{pol}}/T_{\text{cmb}}$
Penzias & Wilson 1965.....	4.0	Scattered	0.1
Caderni et al. 1978.....	100–600	Near Galactic center	0.001–0.01
Nanos 1979.....	9.3	Declination = +40°	$6 \times 10^{-4}$
Lubin & Smoot 1979.....	33	Declinations 38°, 53°, 63°	$3 \times 10^{-4}$
Lubin & Smoot 1981.....	33	11 declinations, –37° to +63°	$6 \times 10^{-5}$
Partridge et al. 1988.....	5	43' × 43' region, declination 80°	$4 \times 10^{-5}$
Wollack et al. 1993.....	26–36	Degree scales, about NCP	$9 \times 10^{-6}$
Netterfield et al. 1995.....	26–46	Degree scales, about NCP	$6 \times 10^{-6}$

and the *Planck Surveyor* will produce full-sky anisotropy maps and are expected to achieve the required sensitivity level to measure polarization as well. The projected sensitivity levels will allow for per-pixel detections of anisotropy with signal-to-noise ratios  $> 1$ . The polarization maps from these missions, however, are expected to have signal-to-noise ratios  $< 1$  for each beam-sized pixel and will be of lower resolution than the anisotropy maps. Fortunately, polarization observations are also possible from the ground; as we will demonstrate, polarized atmospheric emission is expected to be negligible.

This paper will concentrate on strategies for a near-term, ground-based polarization experiment, Polarization Observations of Large Angular Regions (POLAR), optimized to measure CMB polarization at  $7^\circ$  scales for  $\sim 36$  pixels. The design incorporates many techniques developed for previous anisotropy and polarization experiments from the ground, balloons, and space. The primary goal of the paper is to describe the feasibility of measuring large angular scale polarization and to highlight the conclusions that could be drawn from such a measurement. In § 2 we review the theory of CMB polarization that motivates the experimental design. We describe the main experimental challenges in § 3 and focus on two that affect the global design of the instrument: discrimination of CMB polarization from polarized foreground sources (in §§ 4 and 5) and an observing strategy designed to minimize the time required to detect a cosmological signal (§ 6). Finally, we estimate the polarization signal we expect in several different cosmological scenarios and speculate on the conclusions that could be drawn from such detections.

## 2. CMB POLARIZATION: THEORY

Anisotropy of the CMB is generated by metric perturbations of the universe. There are two primary types of perturbation that generate anisotropy of the CMB: scalar contributions, generated by matter-density and radiation-density inhomogeneities; and tensor contributions, associated with gravitational waves. Both types of perturbation give rise to temperature fluctuations in the CMB via the Sachs-Wolfe effect (Sachs & Wolfe 1967).

Thomson scattering of anisotropic radiation by free electrons inevitably generates polarization (Chandrasekhar 1960). Scattering by a single electron produces polarized radiation with an intensity of approximately 10% of the anisotropy quadrupole amplitude when averaged over all directions of photon incidence and scattering. In the case of CMB polarization, the exact polarization level and the angular scale of the distribution of polarization on the sky depend on the optical depth along the observer's line of sight and on the particular sources of metric perturbation (Rees 1968; Basko & Polnarev 1980; Negroponte & Silk

1980; Tolman 1985). For recent reviews, see Hu (1995) and Kosowsky (1996).

According to the standard model of the evolution of the pregalactic medium after recombination, the previously ionized plasma formed neutral hydrogen that was transparent to the CMB. However, the universe may have undergone a secondary ionization of the recombined hydrogen. Gunn & Peterson (1965) formulate a measurement of the ionization fraction of the intergalactic medium using the lack of a Ly $\alpha$  trough in the observed spectra of distant quasars. Recent results show that the majority of intergalactic hydrogen to a redshift of at least  $z \sim 5$  is highly ionized, indicating that the universe must have reionized at an earlier epoch (Peebles 1993). Several models predict that reionization occurred in the redshift range approximately  $30 < z_{\text{ri}} < 70$  (Ozernoi & Chernomordik 1975; Gooding et al. 1991; Durrer 1994; Tegmark & Silk 1993; Nasel'skii & Polnarev 1987).

In contrast to the standard model of recombination, non-standard models invoke additional nonequilibrium sources of ionization. These models predict a prolonged, or even nonexistent, recombination and/or subsequent ionization of the recombined plasma. Since polarization is generated by scattering of photons on free electrons, its magnitude and spatial distribution could be used to discriminate between nonstandard models and the standard model (Bond & Efstathiou 1984, 1987; Basko & Polnarev 1980; Nasel'skii & Polnarev 1987; Ng & Ng 1996; Zaldarriaga & Harari 1995; Crittenden, Davis, & Steinhardt 1993; Frewin, Polnarev, & Coles 1994). An early reionization effectively introduces an additional “last” scattering surface. This has two effects, both of which, in principle, can enhance the magnitude of the polarization on large angular scales. Primarily, the additional scattering of photons during reionization can create new polarized radiation or amplify that already existing via the Thomson mechanism discussed above. Additionally, the second last scattering surface occurs at a much lower redshift, implying that the causal horizon on this rescattering surface is larger and, thus, will subtend a larger angle on the sky today.

In general, large-scale polarization is enhanced in models that predict early reionization. As we will demonstrate, for reasonable nonstandard models, the amplitude of polarization on  $10^\circ$  angular scales is on the level of 10% of the anisotropy while, for the standard model of recombination, the corresponding polarization level does not exceed 1%. It is worth mentioning that all of these models predict approximately the same level of anisotropy at  $10^\circ$  scales, and hence all of them are compatible with the results of the *COBE* DMR experiment.

In the remainder of this section, we will illustrate the important theoretical features of the polarization of the

CMB. We will first describe an analytic treatment that predicts the level of polarization for both standard and non-standard reionization histories. In § 2.3 we will describe a numerical simulation of the effect of a nonstandard reionization history on the polarization of the CMB. We will find that the more qualitative analytic results agree quite well with the quantitative results of our numerical simulations.

### 2.1. Polarization Produced by Cosmological Perturbations

Here we develop the mathematical formalism that will allow us to describe the polarization of the CMB in a consistent fashion. With these tools and using two different techniques, we will subsequently determine the polarization signal we expect to observe. The first method is an analytic approach that will provide a physical framework for understanding the polarization of the CMB. The second approach is more quantitative and will allow us to obtain numerical estimates of the polarization signal. In order to describe the polarization of the CMB, we will first introduce a parameterization that describes the polarization state of arbitrary radiation fields. We then apply this formalism to the polarization state of the cosmological signal that we are seeking to detect.

Consider a polarized electromagnetic wave with angular frequency  $\omega$ :  $\mathbf{E} = E_{y0} \sin(\omega t - \delta_y)\hat{y} + E_{x0} \sin(\omega t - \delta_x)\hat{x}$ . The polarization state of electromagnetic radiation can be characterized by the Stokes parameters  $I$ ,  $Q$ ,  $U$ , and  $V$ .  $I = I_y + I_x$ , with  $I_y = \langle E_{y0}^2 \rangle$  and  $I_x = \langle E_{x0}^2 \rangle$ .  $I$  is the total intensity of the radiation and is always positive. The parameters  $Q = I_y - I_x$  and  $U = 2E_{y0}E_{x0} \cos(\delta_y - \delta_x)$  quantify the linear polarization of the wave, and  $V$  quantifies the degree of circular polarization (when  $V = 0$ , the radiation is linearly polarized or unpolarized). The level of polarization is defined as  $\Pi = (Q^2 + U^2 + V^2)^{1/2}/I$ , and the polarized intensity is  $I_{\text{pol}} \equiv \Pi \times I$ .

An alternate representation for the Stokes parameters will be of use in the following sections. We introduce a symbolic vector for the distribution function of occupation numbers of polarized radiation:  $\hat{\mathbf{n}} = (c^2/h\nu^3)\hat{\mathbf{I}}$ , where  $\hat{\mathbf{I}}$  is the symbolic vector introduced in Chandrasekhar (1960) and is related to the Stokes parameters in the following way:

$$\hat{\mathbf{I}} = \begin{pmatrix} I_x \\ I_y \\ U \\ V \end{pmatrix}.$$

Since Thomson scattering cannot produce circular polarization,  $V = 0$ , we will consider the 3-vector

$$\hat{\mathbf{I}} = \begin{pmatrix} I_x \\ I_y \\ U \end{pmatrix}.$$

An unpolarized distribution in zeroth order approximation is given by

$$\hat{\mathbf{n}}_0 = n_0 \begin{pmatrix} 1 \\ 1 \\ 0 \end{pmatrix}.$$

As shown in Basko & Polnarev (1980) and further discussed in Polnarev (1985) and Zaldarriaga & Harari (1995), polarized radiation in the presence of cosmological pertur-

bations can be represented as

$$\hat{\mathbf{n}} = n_0 \begin{bmatrix} 1 \\ 1 \\ 0 \end{bmatrix} + \hat{\mathbf{n}}_1, \quad (1)$$

where  $\hat{\mathbf{n}}_1 = \hat{\mathbf{n}}_A + \hat{\mathbf{n}}_{\Pi}$  is the correction to the uniform, isotropic, and unpolarized radiation described by  $\hat{\mathbf{n}}_0$ . The Planck spectrum,  $\hat{\mathbf{n}}_0$ , depends only on frequency, and  $\hat{\mathbf{n}}_A + \hat{\mathbf{n}}_{\Pi}$  are the anisotropic and polarized components, respectively, which are functions of the conformal time  $\eta$ , the comoving spatial coordinates  $x^a$ , the photon frequency  $\nu$ , and the photon propagation direction specified by the unit vector  $\hat{\mathbf{e}}(\theta, \phi)$  with the polar angle  $\theta$  and the azimuthal angle  $\phi$  given in an arbitrarily oriented spherical coordinate system.

The equation of radiative transfer in terms of  $\hat{\mathbf{n}}(\eta, x^a, \nu, \mu, \phi)$ , where  $\mu = \cos \theta$ , is

$$\frac{\partial \hat{\mathbf{n}}}{\partial \eta} + e^a \cdot \frac{\partial \hat{\mathbf{n}}}{\partial x^a} = -\frac{\partial \hat{\mathbf{n}}}{\partial \nu} \frac{\partial \nu}{\partial \eta} - q(\hat{\mathbf{n}} - \hat{\mathbf{J}}) \quad (2)$$

and

$$\hat{\mathbf{J}} = \frac{1}{4\pi} \int_{-1}^{+1} \int_0^{2\pi} \mathbf{P}(\mu, \phi, \mu', \phi') \hat{\mathbf{n}}(\eta, x^a, \nu, \mu', \phi') d\mu' d\phi', \quad (3)$$

where  $q = \sigma_T N_e a$  and the Einstein summation convention is implied. In these expressions,  $a$  is the cosmological scale factor,  $\mathbf{P}$  is the scattering matrix described by Chandrasekhar (1960),  $\sigma_T$  is the Thomson cross section, and  $N_e$  is the comoving number density of free electrons. In general, the effects of a particular choice of metric perturbation are manifest in the first term on the right-hand side of equation (2),

$$\frac{\partial \nu}{\partial \eta} = \frac{1}{2} \frac{\partial h_{\alpha\beta}}{\partial \eta} e^\alpha e^\beta \nu$$

(Sachs & Wolfe 1967). After retaining terms up to first order in metric perturbations,  $h_{\alpha\beta}$ , and since  $\partial \nu / \partial \eta$  is of the first order, we can replace  $\partial \hat{\mathbf{n}} / \partial \nu$  with  $\partial \hat{\mathbf{n}}_0 / \partial \nu_0$  in the source term ( $\nu_0$  is the unperturbed frequency). This implies that the factor

$$\gamma = \frac{\nu_0}{n_0} \frac{dn_0}{d\nu_0} = \frac{d \ln n_0}{d \ln \nu_0}$$

gives a universal frequency dependence for anisotropy and polarization effects, independent of the type of metric perturbations (Basko & Polnarev 1980).

The angular dependence of  $\mathbf{P}$  is such that

$$\frac{1}{4\pi} \int_{-1}^{+1} \int_0^{2\pi} \mathbf{P}(\mu, \phi, \mu', \phi') \hat{\mathbf{n}}_0 d\mu' d\phi' = \hat{\mathbf{0}}, \quad (4)$$

where  $\hat{\mathbf{0}}$  is the symbolic 0-vector, so we conclude that, in the zeroth order approximation,  $\hat{\mathbf{J}} = \hat{\mathbf{0}}$ . For the first order approximation in the following, we will understand that  $\hat{\mathbf{J}}$  actually represents  $\hat{\mathbf{J}}_1$ , in which  $\hat{\mathbf{n}}$  is replaced by  $\hat{\mathbf{n}}_1$ .

After linearization and spatial Fourier transformation, the equation of transfer takes the following form (with  $\nu_0$  replaced by  $\nu$ ):

$$\frac{\partial \hat{\mathbf{n}}_{1\mathbf{k}}}{\partial \eta} + ik\mu \hat{\mathbf{n}}_{1\mathbf{k}} = \gamma H_{\mathbf{k}} - q(\hat{\mathbf{n}}_{1\mathbf{k}} - \hat{\mathbf{J}}_{\mathbf{k}}). \quad (5)$$

Here,  $H_{\mathbf{k}} = -\frac{1}{2}\dot{h}_{\alpha\beta\mathbf{k}} e^\alpha e^\beta$ , and the overdot  $\equiv d/d\eta$ . We have specified spherical coordinates in such a way that  $\mu = \cos \theta$ , where  $\theta$  is the angle between a vector  $\hat{e}$  along the line of sight and the wavevector  $\mathbf{k}$ , and where  $\phi$  is the azimuthal angle of the vector  $\hat{e}$  in the plane perpendicular to the vector  $\mathbf{k}$ .

For a given  $\mathbf{k}$ ,  $h_{\alpha\beta\mathbf{k}}$  can be represented as a superposition of scalar waves (below, we will use subscript “ $S$ ”) and tensor gravitational waves (subscript “ $T$ ”). Taking into account the tensorial structure of the waves and restricting our consideration to perturbations with wavelengths longer than the cosmological horizon at the moment of equipartition (i.e., at the moment when the energy density of matter equals that of radiation; see, e.g., Harari & Zaldarriaga 1993), we can write

$$H_{\mathbf{k}} = \frac{1}{15} \eta k^2 \mu^2 \kappa_S(k) - \frac{3}{2k^3} (1 - \mu^2) \cos 2\phi \frac{d}{d\eta} \times \left[ \frac{1}{\eta} \frac{d}{d\eta} \left( \frac{\sin k\eta}{\eta} \right) \right] \kappa_T(k). \quad (6)$$

Here, values of  $[|\kappa_{S,T}(k)|^2]^{1/2}$  are the amplitudes of the corresponding metric perturbations at the moments when their wavelengths are equal to the cosmological horizon.

For  $k\eta \ll 1$ , we have

$$H_{\mathbf{k}} \simeq \frac{1}{15} \eta k^2 \mu^2 \kappa_S(k) - \frac{3}{2} (1 - \mu^2) \cos 2\phi \kappa_T(k), \quad (7)$$

while for  $k\eta \gg 1$ ,

$$H_{\mathbf{k}} = \frac{1}{15} \eta k^2 \mu^2 \kappa_S(k) + \frac{3}{k\eta^2} (1 - \mu^2) \cos 2\phi \cos k\eta \kappa_T(k). \quad (8)$$

For a plane wave perturbation with wavevector  $\mathbf{k}$ , the anisotropy and polarization can be described as (Basko & Polnarev 1980)

$$\hat{n}_A = \alpha_S \left( \mu^2 - \frac{1}{3} \right) \begin{pmatrix} 1 \\ 1 \\ 0 \end{pmatrix} + \frac{\alpha_T}{2} (1 - \mu^2) \begin{pmatrix} 1 \\ 1 \\ 0 \end{pmatrix} \cos 2\phi \quad (9)$$

and

$$\hat{n}_\Pi = \beta_S (1 - \mu^2) \begin{pmatrix} 1 \\ -1 \\ 0 \end{pmatrix} + \beta_T \begin{bmatrix} (1 + \mu^2) \cos 2\phi \\ -(1 + \mu^2) \cos 2\phi \\ 4\mu \sin 2\phi \end{bmatrix}. \quad (10)$$

Substituting equations (9) and (10) into the integro-differential equation of radiative transfer, equation (2), we obtain the following system of coupled ordinary differential equations for  $\alpha_{S,T}$  and  $\beta_{S,T}$ :

$$\dot{\beta}_{S,T} + \frac{3}{10} q \beta_{S,T} = -\frac{1}{10} q \xi_{S,T} \quad (11)$$

and

$$\dot{\xi}_{S,T} + q \xi_{S,T} = F_{S,T}, \quad (12)$$

where  $\xi_{S,T} = \alpha_{S,T} + \beta_{S,T}$  and  $F_{S,T}$  is the appropriate source function for scalar or tensor perturbations. This system of coupled equations illustrates the intimate relation between anisotropy and the generation of polarization. By integrating this system of equations, we obtain the following

general solution for  $\beta_{S,T}$ :

$$\beta_{S,T} = \frac{1}{7} \int_0^\eta F_{S,T} (e^{-\tau} - e^{-3\tau/10}) d\eta', \quad (13)$$

where  $\tau(\eta, \eta') = \int_{\eta'}^\eta q(x^2) dx^2$  is the optical depth with respect to Thomson scattering.

For wavelengths that are large in comparison with the cosmological horizon at the moment of decoupling,  $\eta_D$  ( $k\eta_D \ll 1$ ), the source function at this moment can be approximated by

$$F_{S,T} = \frac{\gamma}{15} \eta k^2 \begin{cases} \kappa_S(k) \\ -\frac{2}{3} \kappa_T(k) \end{cases}. \quad (14)$$

It can be shown that the source functions are rather insensitive to the exact functional form of the variation of the optical depth with respect to time (Basko & Polnarev 1980; Nasel'skii & Polnarev 1987). These functions are primarily characterized by the epoch and duration of decoupling. Following Zaldarriaga & Harari (1995), we adopt the following approximation for the time variation of the optical depth:

$$d\tau = -\frac{d\eta}{\Delta\eta_D} \tau$$

(for a more detailed discussion, see also Basko & Polnarev 1980; Nasel'skii & Polnarev 1987). Here,  $\Delta\eta_D$  is the characteristic timescale of the duration of decoupling. Approximating the source functions under the integral given in equation (13) by their values at the moment of decoupling  $\eta_D$ , which gives the main contribution to polarization, we have

$$\beta_{S,T} \simeq \frac{1}{7} (F_{S,T})|_D \Delta\eta_D \int_0^\infty (e^{-\tau} - e^{-3\tau/10}) \frac{d\tau}{\tau}. \quad (15)$$

The integral in equation (15) can be evaluated in the following way:

$$\beta_{S,T} \simeq \frac{1}{7} (F_{S,T})|_D \Delta\eta_D \lim_{\epsilon \rightarrow 0} \left( \int_\epsilon^\infty e^{-\tau} \frac{d\tau}{\tau} - \int_{-3\epsilon/10}^\infty e^{-\tau} \frac{d\tau'}{\tau'} \right) = \frac{1}{7} \ln \frac{10}{3} (F_{S,T})|_D \Delta\eta_D. \quad (16)$$

Hence,

$$\hat{n} = -\frac{1}{105} \ln \frac{10}{3} \eta_D \Delta\eta_D k^2 \gamma \times \left\{ \frac{1}{2} \kappa_S(k) (1 - \mu^2) \begin{pmatrix} 1 \\ -1 \\ 0 \end{pmatrix} - \frac{3}{4} \kappa_T(k) \begin{bmatrix} (1 + \mu^2) \cos 2\phi \\ -(1 + \mu^2) \cos 2\phi \\ 4\mu \sin 2\phi \end{bmatrix} \right\}. \quad (17)$$

Comparing equation (17) with equation (10), we find that the polarization generated by a single perturbation mode with wavevector  $\mathbf{k}$  is given by

$$\Pi_{\mathbf{k}} = -\frac{2}{105} \ln \frac{10}{3} (\eta_D k) (\Delta_D k) \gamma \times \{ \kappa_S(k) (1 - \mu^2) - \frac{3}{4} \kappa_T(k) [(1 + \mu^2) \cos 2\phi + 2\mu \sin 2\phi] \}. \quad (18)$$

Now we can calculate the root mean square (rms) polarization measured by an antenna with an effective averaging angle  $\Theta_A$ . The main contribution to the rms polarization,  $\Pi(\Theta_A)$ , is contributed by modes with  $k < k_{\max}(\Theta_A) \approx 2\pi/\Theta_A = 360^\circ/\Theta_A$ :

$$\Pi(\Theta_A) = \sqrt{\langle \Pi^2 \rangle_{k > 2\pi/\Theta_A}} \quad (19)$$

and

$$\Pi(\Theta_A) = \frac{2}{105} \ln \frac{10}{3} \eta_D \Delta \eta_D \gamma \sqrt{Q_S B_S + Q_T B_T}, \quad (20)$$

where

$$B_S = \int_{-1}^1 (1 - \mu^2)^2 d\mu = \frac{16}{15} \quad (21)$$

and

$$B_T = \frac{9}{8\pi} \left[ \int_{-1}^1 (1 + \mu^2)^2 \int_0^{2\pi} \cos^2 2\phi d\phi + \int_{-1}^1 4\mu^2 d\mu \int_0^{2\pi} \sin^2 2\phi \right] = \frac{36}{5}. \quad (22)$$

Here  $Q_{S,T} = \int_0^{k_{\max}(\Theta_A)} k^4 |\kappa_{S,T}(k)|^2 dk/k$ , with  $|\kappa_{S,T}(k)|^2 = \kappa_{0S,T} k^{ns,T}$ , and  $(|\kappa_{0S,T}|^2)^{1/2}$  are the amplitudes of perturbations with wavelengths equal to the cosmological horizon at the present moment ( $n=0$  corresponds to a scale-invariant Harrison-Zeldovich spectrum). These amplitudes are normalized to the *COBE* DMR anisotropy quadrupole detection that is approximately equal to  $2 \times 10^{-5}$ . Assuming that  $n_S = n_T = n$ , we obtain

$$\Pi(\Theta_A) = \frac{8}{105\sqrt{15}} \ln \frac{10}{3} \eta_D \Delta \eta_D \frac{1}{\sqrt{4+n}} \times \left( \frac{360^\circ}{\Theta_A} \right)^{2+n/2} \gamma \sqrt{\kappa_{0S}^2 + \frac{27}{4} \kappa_{0T}^2}. \quad (23)$$

Taking into account the relationship between redshift and conformal time,  $z \sim \eta^{-2}$ , we have  $\Delta z_D/z_D \sim 2 \Delta \eta_D/\eta_D$ ; hence

$$\eta_D \Delta \eta_D \simeq \eta_D^2 \frac{\Delta \eta_D}{\eta_D} = \frac{1}{2} \frac{\Delta z_D}{z_D} = \frac{1}{2} \frac{\Delta z_D}{z_D} \frac{1}{z_{SD}} \left( \frac{z_{SD}}{z_D} \right),$$

where  $z_{SD}$  is the redshift of decoupling predicted by the standard model of recombination. Finally,

$$\Pi(\Theta_A) = 4 \times 10^{-7} \frac{\Delta z_D}{z_D} \left( \frac{z_{SD}}{z_D} \right) \left( \frac{7^\circ}{\Theta_A} \right)^{2+n/2} \gamma \aleph_{n,g}, \quad (24)$$

where

$$\aleph_{n,g} = \frac{2 \times 10^{-2} \ln(10/3)}{105\sqrt{15}} \left( \frac{7^\circ}{360^\circ} \right)^2 \frac{\sqrt{\kappa_{0T}^2 + \kappa_{0S}^2}}{2 \times 10^{-5}} \frac{10^3}{z_{SD}} \times \left( 1 + \frac{n}{4} \right)^{-1/2} \left( \frac{360^\circ}{7^\circ} \right)^{n/2} \sqrt{\frac{1 + 27g^2/8}{1 + g^2}}, \quad (25)$$

and

$$g = \frac{\kappa_{0T}}{\kappa_{0S}}$$

is the ratio of the tensor perturbation amplitudes to the scalar amplitudes.

The factor  $\aleph_{n,g}$  incorporates the perturbation amplitudes, normalized to the anisotropy quadrupole measured by the

*COBE* DMR. It contains all information about the type of metric perturbation, allowing us to isolate factors that depend upon the nature of the perturbations and those that do not. For  $n=0$  and  $g=0$  (i.e., no tensor perturbations),  $\aleph_{0,g} \simeq 1$ . When  $g=\infty$  (i.e., no scalar perturbations),  $\aleph_{0,g} \simeq 1.84$ . Finally, when  $g=1$  (i.e., equal tensor and scalar contributions), we find  $\aleph_{0,g} \simeq 1.47$ . From this, we observe that  $\aleph_{n,g}$  is rather insensitive to  $g$ , the ratio of tensor to scalar amplitudes.

We now emphasize the angular regions to which the preceding discussion is relevant. Equations (23), (24), and (25) (which are based on asymptotic eq. [7] and the approximations used in eq. [15]) are valid for modes that satisfy  $k\Delta\eta_D < 1$ . In terms of angle on the sky,

$$\frac{360^\circ}{\Theta_A} \frac{\Delta \eta_D}{\eta_D} \eta_D < 1.$$

We can apply equations (23), (24), and (25) to an observation that has an angular resolution  $\Theta_A$  as long as

$$\Theta_A > \Theta_{A\min} = 60^\circ \frac{1}{2} \frac{\Delta z_D}{z_D^{3/2}} = \frac{180}{z_{SD}^{1/2}} \left( \frac{\Delta z_D}{z_D} \right) \left( \frac{z_{SD}}{z_D} \right)^{1/2} \simeq 6^\circ \frac{\Delta z_D}{z_D} \left( \frac{z_{SD}}{z_D} \right)^{1/2} \left( \frac{\Delta z_{SD}}{10^3} \right)^{-1/2}.$$

As an example, the standard model of recombination predicts  $\Delta z_D/z_D \simeq 0.1$ , which implies that  $\Theta_{A\min} \simeq 0.6^\circ$ . For pure scalar perturbations ( $n=0$ ), the expected level of polarization at this angular scale is  $\Pi(0.6^\circ) \simeq 6 \times 10^{-6}$ . For an observation with  $\Theta_A \simeq 6^\circ$ , the polarization is  $\Pi(6^\circ) \simeq 5 \times 10^{-8}$ . The observed polarization is suppressed by a factor of  $\sim 100$  with this lower resolution beam.

Consider another example, a nonstandard model for which  $\Delta z_D/z_D \simeq 1$ ,  $z_D \simeq z_{SD}$ , and the angular scale is  $\Theta_{A\min} \simeq 6^\circ$ . The polarization predicted in this scenario is  $\Pi(6^\circ) \simeq 5 \times 10^{-7}$ . Finally, for  $\Theta_A < \Theta_{A\min}$ , the polarization is suppressed, and its dependence on  $\Theta_A$  is determined by the details of its ionization history (Zaldarriaga 1997; Polnarev 1985; Nasel'skii & Polnarev 1987; Bond & Efstathiou 1984, 1987).

To summarize, for a given  $\Theta_A$ , the polarization level is proportional to  $\Delta z_D/z_D$  (see eq. [24]) and is smallest for the standard model of recombination. Alternatively, this analytic approximation applies to smaller angles in the standard model, as opposed to the larger angles predicted by nonstandard models (see Nasel'skii & Polnarev 1987 for a more detailed discussion). Figure 1 schematically illustrates the angular dependence of polarization in standard and nonstandard models.

## 2.2. Polarization Power Spectrum

The analytic treatment above describes the essential physics responsible for the generation of CMB polarization. We have discussed the aspects of nonstandard recombination that are relevant to the large-scale polarization of the CMB. In order to estimate the observable polarization signature, we now detail a more quantitative approach based on the polarization power spectrum. This approach also allows us to discuss the effect of an early reionization on the observed polarization.

For quantitative estimates, the polarization and anisotropy source terms that appear in the equation of transfer can be decomposed into Legendre series. The individual

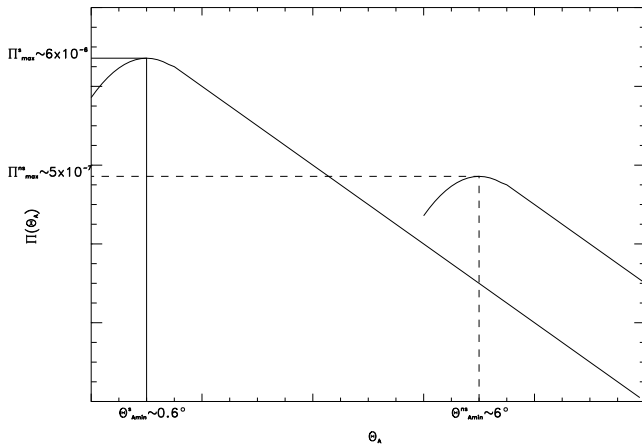


FIG. 1.—Schematic dependence of CMB polarization on angular scale and recombination scenario. In nonstandard models that predict a prolonged recombination, the angular scale and the level of polarization are larger than for standard models.

modes are then evolved to the present where the spatial structure of the CMB can be computed (see, e.g., Bond & Efstathiou 1984, 1987; Ng & Ng 1995; Zaldarriaga & Harari 1995; Freun et al. 1994). Because the CMB is an imprint of the epoch of linear evolution of perturbations, the individual modes evolve more or less independently. This treatment lends itself particularly well to numerical analysis (Seljak & Zaldarriaga 1996). The relevant results of such analysis to the present discussion are the anisotropy and polarization power spectra. Here we connect the results of these numerical procedures with the analytic treatment presented in the previous subsection.

The temperature of the CMB, being a scalar-valued function, can be expanded in a spherical harmonic series on the sky at a particular point on the sky,  $\hat{x}$ :

$$T(\hat{x}) = \sum_{\ell, m} a_{T, \ell m} Y_{\ell m}(\hat{x}), \quad (26)$$

where  $Y_{\ell m}(\hat{x})$  are the spherical harmonics at  $\hat{x}$ . The temperature two-point correlation function is given by

$$C_{T, \ell} = \frac{1}{2\ell + 1} \sum_m \langle a_{T, \ell m}^* a_{T, \ell m} \rangle. \quad (27)$$

The variance of  $a_{T, \ell m}$  is given by  $C_{T, \ell}$ , since  $\text{Var}[a_{T, \ell m}] = \langle |a_{T, \ell m}|^2 \rangle - \langle |a_{T, \ell m}| \rangle^2 = \langle |a_{T, \ell m}|^2 \rangle \equiv C_{T, \ell}$  if the  $a_{T, \ell m}$  are Gaussian-distributed with zero mean and  $\langle \dots \rangle$  denotes a whole-sky average followed by an average over all observational positions.

The polarization of the CMB is a tensor-valued function with a symmetry group different from that of the anisotropy. As shown in Zaldarriaga & Seljak (1997), complex linear combinations of the Stokes parameters transform under rotation about the line of sight by an angle  $\psi$  as

$$(Q \pm iU)(\hat{x}) = \exp^{\mp 2i\psi} (Q \pm iU)(\hat{x}). \quad (28)$$

The expressions analogous to equation (26) for the Stokes parameters are

$$(Q + iU)(\hat{x}) = \sum_{\ell, m} a_{2, \ell m}^{\Pi} Y_{\ell m}(\hat{x}) \quad (29)$$

and

$$(Q - iU)(\hat{x}) = \sum_{\ell, m} a_{-2, \ell m}^{\Pi} Y_{\ell m}(\hat{x}), \quad (30)$$

where the spin-weighted spherical harmonics,  $_{-2}Y_{\ell m}$ , are a complete and orthonormal set of basis functions on the sphere (for an equivalent technique that uses second-rank tensors on the sphere to describe the Stokes parameters, see Kamionkowski et al. 1998). Taking complex linear combinations of the expansion coefficients  $a_{\pm 2, \ell m}^{\Pi}$ , one defines

$$a_{E, \ell m} \equiv -(a_{2, \ell m}^{\Pi} + a_{-2, \ell m}^{\Pi})/2 \quad (31)$$

and

$$a_{B, \ell m} \equiv i(a_{2, \ell m}^{\Pi} - a_{-2, \ell m}^{\Pi})/2. \quad (32)$$

From these we construct two independent correlation functions that characterize the polarization,

$$C_{E, \ell}^{\Pi} = \frac{1}{2\ell + 1} \sum_m \langle a_{E, \ell m}^* a_{E, \ell m} \rangle \quad (33)$$

and

$$C_{B, \ell}^{\Pi} = \frac{1}{2\ell + 1} \sum_m \langle a_{B, \ell m}^* a_{B, \ell m} \rangle. \quad (34)$$

$C_{E, \ell}^{\Pi}$  and  $C_{B, \ell}^{\Pi}$  have different physical origins and have interesting properties under symmetry transformations, such as parity inversion. We refer to Seljak & Zaldarriaga (1998) for further discussion of these fascinating spectra.

We now define  $C_{\ell}^{\Pi} \equiv C_{E, \ell}^{\Pi} + C_{B, \ell}^{\Pi}$  and form

$$\langle Q(x_1)Q(x_2) + U(x_1)U(x_2) \rangle = \frac{1}{4\pi} \sum_{\ell=2}^{\infty} (2\ell + 1) C_{\ell}^{\Pi} P_{\ell}(\cos \theta), \quad (35)$$

where  $x_1$  and  $x_2$  are vectors toward two different locations on the sky separated by an angle  $\theta$ . When  $\theta = 0$ , we have for the polarization autocorrelation

$$I_{\text{pol}}^2 = \langle Q^2 + U^2 \rangle = \frac{1}{4\pi} \sum_{\ell=2}^{\infty} (2\ell + 1) C_{\ell}^{\Pi}.$$

We can now connect the results of this power spectrum calculation with the analytic treatment presented above. For a measurement of the polarization at an angular scale  $\Theta_A$ , we have for the observable level of polarization

$$\Pi(\Theta_A) \equiv \frac{I_{\text{pol}}}{I} = \frac{1}{I} \sqrt{\frac{1}{4\pi} \sum_{\ell=2}^{\infty} (2\ell + 1) W_{\ell}^{\Theta_A} \times C_{\ell}^{\Pi}}, \quad (36)$$

where  $I \simeq 2.7$  K and the window function,  $W_{\ell}^{\Theta_A}$ , is a factor that weights the contribution of the  $\ell$ th moment to the power spectrum. It quantifies the angular sensitivity of a given experiment (see § 6 for further detail). For a given theoretical model (i.e.,  $C_{\ell}$ ), equation (36) can be compared to the analytic expression given in equation (24).

The polarization power spectrum,  $C_{\ell}^{\Pi}$ , is highly dependent on the cosmological details of the model used to generate the anisotropy spectrum,  $C_{\ell}^z$ . For this reason, the ratio of polarization to anisotropy is often calculated in order to predict observable levels of polarization for particular

observations (Ng & Ng 1995; Crittenden et al. 1993). In practice, the polarization spectra are normalized to the appropriate anisotropy spectra, which are in turn normalized to the low  $\ell$  values of  $C_\ell^a$  measured by the *COBE* DMR. The power spectra are generated numerically by CMBFAST (Seljak & Zaldarriaga 1996), which permits simultaneous calculation of anisotropy and polarization as well as consistent normalization.

### 2.3. The Effect of Reionization on the Polarization Power Spectrum

As mentioned earlier, nonstandard models of the ionization history are characterized by noninstantaneous decoupling and/or nonzero optical depth along CMB photon trajectories. We have discussed the effect of noninstantaneous recombination using the analytic method treated above. We now wish to examine the effect of reionization on the details of the polarization of the CMB. This investigation lends itself particularly well to the numerical evaluation of the polarization power spectrum, calculated using numerical routines such as CMBFAST.

In general, models of reionization often rely on structures such as an early generation of stars (Population III) and energetic protogalaxies to provide either ionizing radiation or collisional heating mechanisms. Thus, every model of reionization corresponds to a structure-formation scenario, as well as to a commensurate set of cosmological parameters to be confronted with observational evidence. We will not speculate here on the plausibility of specific models of reionization. Discussion of mechanisms for early reionization can be found in Ozernoi & Chenomordik (1975), Gooding et al. (1991), Durrer (1994), Tegmark & Silk (1993), and Nasel'skii & Polnarev (1987). As noted above, the Gunn-Peterson test provides definitive evidence for an ionized intergalactic medium out to a redshift of at least  $z = 5$ . In fact, the upper limit on the redshift of reionization is set only by the paucity of observed quasars beyond  $z = 5$  and, in principle, could be much higher than this. The *COBE* FIRAS limit on the Compton  $y$ -parameter  $y = \int dt k_b (T_e - T_{\text{CMB}}) / m_e c^2 \leq 2.5 \times 10^{-5}$  (Fixsen et al. 1996) severely restricts the energy input allowed in models of reionization but does not tightly constrain the epoch of reionization or the ionized fraction of the intergalactic medium. The limit is compatible with many early reionization scenarios.

The effect of reionization can be parameterized in two equivalent forms. One method is specified by the optical depth for photons,  $\tau_{\text{ri}}$ , caused by Thomson scattering along a line of sight to the last scattering surface. The second method specifies the redshift of reionization,  $z_{\text{ri}}$ , and the fractional ionization,  $x$  (the electron-to-proton ratio). The two parameterizations are related as follows (Peebles 1993):

$$\tau_{\text{ri}} = 0.0015 \left( \frac{x}{1} \right) \frac{\Omega_B}{0.05} \left( \frac{\Omega}{1} \right)^{-1/2} \left( \frac{h}{0.65} \right) (1 + z_{\text{ri}})^{3/2}, \quad (37)$$

where  $h$  is the Hubble parameter,  $\Omega$  is the total density parameter of the universe, and  $\Omega_B$  is the density parameter of baryonic matter. Equation (37) shows the effect of the curvature of the universe on the optical depth. For reionization occurring at the same redshift and ionization fraction, the optical depth in an open universe ( $\Omega < 1$ ) will be greater than in a flat or closed universe. We also note that the physical size of regions that are in causal contact (Hubble

radius) at the epoch of reionization,  $t_{\text{ri}}$ , is of order  $\sim ct_{\text{ri}}$ . We expect that regions of this size will produce coherent polarization of the CMB and affect the observed polarization power spectrum at angular scales that correspond to the angular scale subtended by the horizon size at the epoch of reionization. This argument is similar to those that predict a coherence scale in the CMB anisotropy power spectrum. For example, the acoustic peaks in the CMB anisotropy power spectrum arise from causal mechanisms (i.e., sound waves propagating in the photon-baryon fluid) acting on scales on the order of the horizon size at the epoch of decoupling. A similar effect occurs for the CMB polarization power spectrum, though in this case it is the horizon size of the rescattering surface, not the “primary” scattering surface, which is imprinted in the observed power spectrum.

Following Peebles (1993), we expect that the observed CMB polarization angular correlation scale will be  $\Theta_{\text{ri}} \sim 0.1(\Omega_B \Omega h)^{1/3}$  rad. For  $\Omega = 0.1$ ,  $\Omega_B = 0.1$ , and  $h = 1$ , we find  $\Theta_{\text{ri}} \sim 1^\circ$ , and for  $\Omega = 1$ ,  $\Omega_B = 0.05$ , and  $h = 0.65$ , we find  $\Theta_{\text{ri}} \sim 2^\circ$ . This new angular scale, absent in nonreionized models, is manifested in the spatial polarization correlation function and creates a peak in the reionized polarization power spectra at  $\ell \leq 20$ .

Using CMBFAST, we have generated polarization spectra created by scalar perturbations in a cold dark matter-dominated (CDM-dominated) completely reionized universe with  $x = 1$ ,  $\Omega = 1$ ,  $\Omega_B = 0.05$ , and  $h = 0.65$ . By varying the redshift of reionization in the range  $0 < z_{\text{ri}} < 105$ , we compute multiple polarization power spectra, which are displayed in Figure 2. The power spectra illustrate the main features expected from the theoretical principles detailed above. Large angular scales correspond to modes with wavelengths greater than the width of the last scattering surface. Prior to recombination, photons and baryons are tightly coupled and the relatively short time-scale for acoustic oscillations prevents the formation of long-wavelength perturbations. These effects are particularly evident in models without reionization.

In models with early reionization, polarization at large angular scales is enhanced because of multiple photon scatterings following reionization. At smaller angular scales ( $\ell \sim 100$ ) in models with and without reionization, the

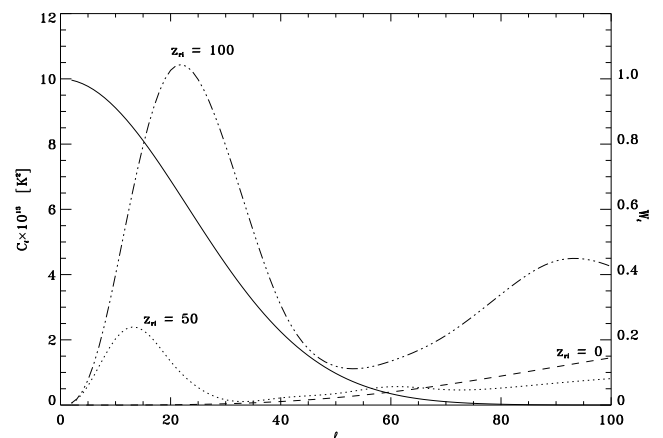


FIG. 2.—Polarization power spectra and window function for POLAR. Three spectra are displayed for a CDM ( $\Omega = 1$ ,  $\Omega_B = 0.05$ ,  $H = 65$ ) universe with three different redshifts of reionization ( $z_{\text{ri}} = 0, 50$ , and  $100$ ). Also shown (solid line) is the single-beam window function of POLAR.

polarization power spectra exhibit oscillatory behavior, caused by the same type of acoustic oscillations that generate the Doppler peaks in the anisotropy power spectra (Frewin et al. 1994; Zaldarriaga 1997). Though not relevant for the large angular scale considerations discussed here, for  $\ell \gg 100$ , the polarization is highly suppressed because of Silk damping (Hu 1995).

The power spectra are, effectively, predictions of the polarization that should be observable given a particular observing strategy. We will show in § 6 that the rms polarization expected from the spectra shown in Figure 2 with  $\Theta_A = 7^\circ$  is in the range  $0.05 < I_{\text{pol}} < 1.0 \mu\text{K}$ , where the lower limit is for standard recombination with no reionization and the upper limit is for total reionization starting at  $z = 105$ . These limits agree well with the analytic estimates for nonstandard ionization histories discussed in § 2.1. For a  $6^\circ$  experiment and a nonstandard ionization history, Figure 1 predicts a polarization level of  $5 \times 10^{-7} \sim 1 \mu\text{K}$ , which agrees well with our numerical simulations of early reionization (e.g., for  $z_{\text{reionization}} = 105$ ).

### 3. EXPERIMENTAL OVERVIEW

Measurement of the polarization of the CMB poses a wide variety of experimental challenges, many of which are familiar from the experiments now measuring spatial anisotropy in the CMB. Below, we describe the design of POLAR to illustrate the experimental issues that must be addressed in any CMB polarization observation.

POLAR will measure polarization on  $7^\circ$  scales with two separate radiometers, one in the  $K_a$  frequency band and one in the  $Q$  band, covering the spectrum between 26 and 46 GHz. These radiometers operate simultaneously, and their frequency bands are multiplexed into several subbands to allow for discrimination against foreground sources. Each radiometer executes a drift scan of the zenith with a separate FWHM =  $7^\circ$  beam produced by a corrugated feed horn antenna. POLAR will observe  $\sim 36$  different pixels for many months to reach the level of a few microkelvins per pixel. The design builds on techniques developed in previous searches for CMB polarization (Nanos 1979; Lubin 1980; Lubin & Smoot 1981; Lubin, Melese, & Smoot 1983; Wollack et al. 1993; Netterfield et al. 1995) and is driven by the key issues identified in this paper, the size and angular scale of the anticipated CMB signals, spectral removal of foreground sources, optimization of the observing scheme, and anticipated systematic effects.

#### 3.1. The Polarimeter

Radiation from the sky couples into a corrugated circular horn antenna (see Fig. 3). This antenna has extremely low sidelobes, near  $-80$  dB at  $90^\circ$  off-axis in both polarizations across a full waveguide band. The main lobe of the antenna is Gaussian with an FWHM of  $7^\circ$ , which is near the minimum that can easily be obtained without additional optical components such as lenses or primary reflectors. The antenna output couples to an ortho-mode transducer (OMT), a waveguide device that decomposes the incoming wave into two orthogonal linear polarization components. The OMT defines the  $x$ - $y$  coordinate system of the antenna.

The  $Q$  and  $U$  Stokes parameters are defined in terms of a coordinate system fixed to the sky. There are several approaches to measuring  $Q$  and  $U$  for a particular pixel on the sky. Lubin & Smoot (1981) employ a Dicke switch that

alternately couples each of the polarization components from the OMT to a low-noise amplifier and square-law detector (Lubin 1980; Lubin & Smoot 1981). Phase-sensitive detection at the modulation frequency of the switch yields the difference between these two components, the  $Q$  Stokes parameter, and helps overcome  $1/f$  noise from the amplifier. One can show that after a  $45^\circ$  rotation about the antenna symmetry axis, the instrument measures the  $U$  parameter. A second technique couples the output of an OMT directly to two square-law detectors (Netterfield et al. 1995; Wollack et al. 1997). The beam is switched on the sky to measure the spatial anisotropy in two orthogonal polarizations. This approach measures the anisotropy in the  $Q$  Stokes parameters of the incident radiation field and provides the most stringent upper limits on the spatial anisotropy of the polarization of the CMB.

An alternate approach, employed in POLAR, is the correlation radiometer (Fujimoto 1964; Rohlf 1990). In this instrument, the two polarization components are amplified in separate parallel amplifier chains; the output signals are correlated, resulting in an IF signal proportional to the  $U$  Stokes parameter. This type of instrument effectively “chops” between the two input RF signals at a frequency that is comparable to that of the RF signals themselves. The correlation polarimeter has a  $2^{1/2}$  noise advantage over the Dicke-switched approach. An advantage of this differencing mechanism is that it has no magnetic or moving parts, which have traditionally complicated experiments of this type. After a  $45^\circ$  rotation, the correlator gives the  $Q$  parameter. POLAR rotates about the vertical in  $45^\circ$  steps at a few rpm. The rotation modulates the output sinusoidally between  $U$  and  $Q$  at twice the rotation frequency and allows the removal of an instrumental offset and of other instrumental effects that are not modulated at this frequency.

The sensitivity of the polarimeter is determined by low-noise HEMT amplifiers cooled to 15 K by a commercial cryocooler. State-of-the-art versions of these amplifiers achieve noise temperatures of  $\sim 10$  K over a bandwidth of  $\sim 10$  GHz in both the  $K_a$  and  $Q$  bands (Pospieszalski 1992, 1995). This noise temperature is comparable to the antenna temperature of the atmosphere at a good observing site. Nevertheless, long integration periods are required to reach a sensitivity level  $\simeq 1 \mu\text{K}$ . The rms noise in a measurement of either  $Q$  or  $U$  (in antenna temperature) is given by the radiometer equation (Krauss 1982). For the  $Q$  Stokes parameter,

$$\Delta Q_{\text{rms}} = \frac{\kappa(T_{\text{rec}} + T_{\text{atm}} + 2.7)}{\sqrt{\Delta\nu\tau/2}}, \quad (38)$$

where  $T_{\text{rec}}$  and  $T_{\text{atm}}$  are the receiver and atmospheric noise temperatures, respectively.  $\tau$  is the total time spent observing the CMB; the time spent observing either  $Q$  or  $U$  is  $\tau/2$ .  $\Delta\nu$  is the RF bandwidth, and  $\kappa = 2^{1/2}$  for a correlation radiometer. For the  $K_a$  polarimeter,  $T_{\text{rec}} \simeq 20$  K,  $T_{\text{atm}} \simeq 10$  K, and  $\Delta\nu$  is 10 GHz, resulting in a sensitivity to  $Q$  or  $U$  of  $NET = \Delta Q_{\text{rms}}(\tau/2)^{1/2} \simeq 460 \mu\text{K s}^{1/2}$ . For the total polarized intensity, we have  $I_{\text{pol}} = (Q^2 + U^2)^{1/2}$ . The error in  $I_{\text{pol}}$  is  $\Delta I_{\text{pol}} = 2^{1/2}\Delta Q_{\text{rms}} = 650 \mu\text{K s}^{1/2}$  before foreground subtraction. To reach a signal level of  $\Delta I_{\text{pol}} = 1 \mu\text{K}$  for a single pixel requires an integration time of  $\sim 120$  hr. Consequently, to measure polarization at a signal-to-noise ratio of 1 pixel $^{-1}$  for all 36 pixels demands a total observation time of

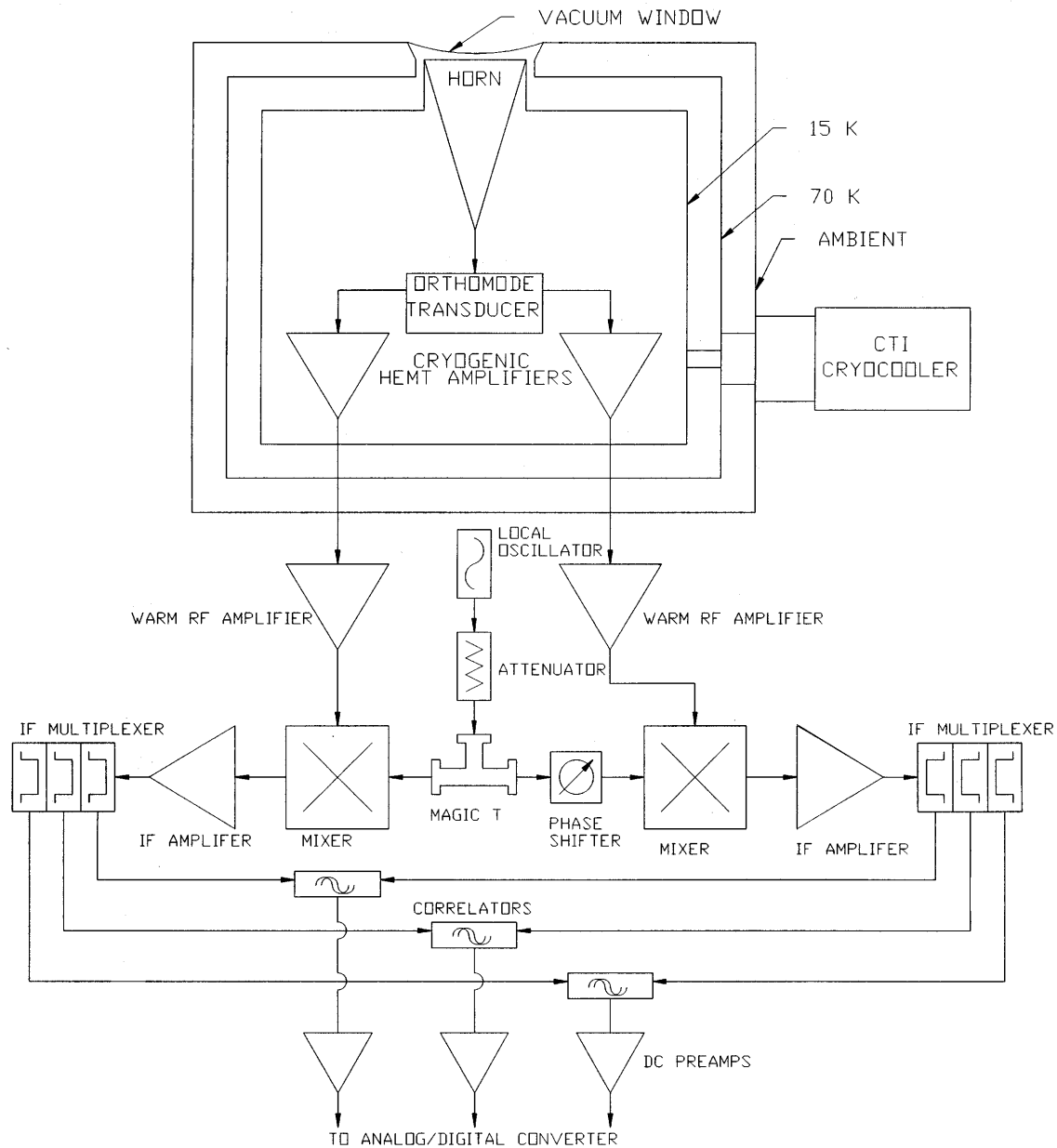


FIG. 3.—POLAR schematic. The correlation polarimeter is a wideband, total-power device. An orthomode transducer separates the two orthogonal linear polarization components of the incident radiation. HEMT amplifiers are cooled to 15K inside a dewar. The remaining components are at ambient temperature.

~180 days. The *Q*-band radiometer requires a similar amount of time.

### 3.2. Systematic Effects

Because the anticipated polarization signal is a factor of ~10 smaller than the temperature anisotropy currently being detected, the understanding of systematic errors is crucial. Polarization experiments have several advantages, however, that promise to make this effort possible. First, the atmosphere is known to be polarized only at a very low level, far below the expected level of CMB polarization (see § 4). Additionally, POLAR is essentially a total (polarized) power radiometer, which eliminates the comparison of pixels through different airmasses and at different times. In anisotropy observations, beam switching often adds noise

and additional chop-dependent signals. Potentially, atmospheric effects will have a smaller contribution to this type of experiment than to ground-based CMB anisotropy experiments and will allow longer observation times than have been possible in the past. Long-term observations are key to understanding and removing systematic effects (Wilkinson 1995; Kogut et al. 1996a; Bennett et al. 1993). Many spurious instrumental effects can be isolated from astrophysical effects by long-term integration tests with the horn antenna replaced by a cold termination.

In Table 2 we list some important systematic effects encountered in previous polarization measurements and summarize the solution adopted by POLAR. A full analysis of all potential effects is obviously beyond the scope of this paper. In § 4 we discuss in detail the discrimination against

TABLE 2  
EXPECTED SYSTEMATIC EFFECTS

Effect	Origin	Removal/Control Method
Mechanical strain <sup>a</sup> .....	Instrument rotation	Vertical drift scan
Magnetic coupling <sup>b</sup> .....	Rotation in Earth's field	No ferrite components
Microphonics <sup>c</sup> .....	Mechanical vibration	Mechanical isolation
Electromagnetic interference <sup>d</sup> .....	Local sources	Shield/filter
Offsets <sup>e</sup> .....	Polarization cross coupling	Isolation/instrument rotation
Radio-frequency interference <sup>f</sup> .....	In-band Sources	Identification and data editing
Thermal variations <sup>g</sup> .....	Diurnal/environment	Temp. control/shielding
Sidelobe pickup <sup>h</sup> .....	Sun/Moon/Earth	Low sidelobe antenna/shielding

<sup>a</sup> A problem with any radiometer that must move in a gravitational field is position-dependent stress and strain on waveguide joints, etc. In POLAR, these problems are minimized by staring at the zenith, so no gravitational torques are present. The rotation speed is slow,  $\sim 1$  rpm, so accelerations on stopping and starting rotation are small.

<sup>b</sup> A particular concern is the coupling of the Earth's magnetic field to the radiometer. The *COBE* DMR had ferrite Dicke switches that produced a spurious signal at the  $\approx 0.1$  mK level (Kogut et al. 1996a). POLAR has no ferrite components, but other components such as amplifiers, etc., may have a low-level magnetic field dependence. Modulation of these effects can be minimized by maintaining a constant orientation of the rotation axis with respect to the Earth's field.

<sup>c</sup> The effects of vibrations that occur during rotation are reduced by taking data while the instrument is stationary and by stiffening the support structures.

<sup>d</sup> This effect can be controlled by Faraday shielding the instrument and by filtering electrical lines.

<sup>e</sup> Cross polarization in the antenna and the OMT create correlated signals in both arms of the polarimeter, which in turn produce an offset signal. If this offset is stable on the timescale of instrument rotation, it is subtracted by phase-sensitive detection at the rotation frequency.

<sup>f</sup> RF sources that occur in the radiometer RF band or IF band are becoming increasingly troublesome. Of particular concern in the future will be communications satellites operating in the bands of interest.

<sup>g</sup> Temperature variations in the radiometer that occur at the rotation rate of the instrument can be mitigated by active temperature control and by shielding the instrument from the Sun. The latter function is naturally performed by the ground shields so that the antenna and receiver are completely shielded.

<sup>h</sup> The polarimeter must be able to reject or discriminate against emission from the Sun, Moon, and Earth, which appear only in the sidelobes of the beam. None of these sources are expected to be significantly polarized, but asymmetry in the antenna response to the two linear polarizations will create spurious signals. Requiring the total power from these sources to lie below  $1 \mu\text{K}$  demands 75 dB and 63 dB sidelobe rejection for the Sun and Moon, respectively. Assuming 20 dB rejection from the ground screen, this level of rejection can be achieved with the corrugated horn antenna (Janssen et al. 1979) if data are rejected when these sources lie closer to the zenith than  $50^\circ$  and  $30^\circ$ , respectively. Binning of the data in Sun-centered or Moon-centered coordinates will allow us to uncover correlations between the position of these objects and the response of the polarimeter.

foreground sources such as extragalactic sources, Galactic sources, and the atmosphere.

#### 4. FOREGROUND SOURCES

A fundamental question for any measurement of the polarization of the CMB is whether the expected signal can be distinguished from polarized foreground sources. While astrophysical (noncosmological) sources of polarized radiation are of interest for other fields, the measurement of CMB polarization is our main objective, so these sources are spurious effects. These foreground sources all have spectra that are distinct from that of the CMB and can in principle be distinguished from it by multifrequency measurements. This technique has been employed for observations of CMB anisotropy (Brandt et al. 1994). However, polarized foreground spectra have not been studied as extensively. To estimate the intensity and spectra of these foreground sources, we rely on theoretical predictions and extrapolations from measurements at different frequencies of the antenna temperatures of these foregrounds. Here we summarize the properties of atmospheric and astrophysical (though noncosmological) foreground sources.

*Synchrotron emission.*—Diffuse Galactic synchrotron radiation arises from ionized regions of our Galaxy that possess magnetic fields. The antenna temperature of synchrotron emission obeys a power law,

$$T_{\text{synchrotron}}(\nu) \propto \nu^\beta,$$

where  $\beta$  is referred to as the “synchrotron spectral index.” The polarization level  $\Pi$  of synchrotron radiation is related to the spectral index (Cortiglioni & Spoelstra 1995),

$$\Pi = \frac{3\beta + 3}{3\beta + 1}.$$

Faraday rotation and nonuniform magnetic fields will reduce the level of polarization given by this equation. Full-sky polarization maps made at radio frequencies (Brouw & Spoelstra 1976) have been extrapolated to millimeter-wave frequencies assuming a power-law spectrum (Lubin & Smoot 1981). The radiation is linearly polarized between approximately 10% and 75%, depending on Galactic coordinates. Below 80 GHz, the polarized synchrotron emission dominates all sources, including the CMB if it is polarized at the  $1 \times 10^{-6}$  level, as shown in Figure 4. We estimate the spectrum of the synchrotron radiation by extrapolating the Brouw & Spoelstra (1976) measurement at 1411 MHz to millimeter wavelengths with the modified power-law spectrum used to fit the *COBE* DMR data (Bennett et al. 1992). For our modeling purposes, we choose  $-2.9 \geq \beta \geq -3.2$  and a total intensity of approximately  $50 \mu\text{K}$  at 30 GHz, typical of high Galactic latitudes (Kogut et al. 1996b; Bennett et al. 1992), and  $\Pi = 75\%$ .

*Bremsstrahlung emission.*—Bremsstrahlung, or free-free, emission from ionized hydrogen (H II) regions is not polarized (Rybicki & Lightman 1979). However, bremsstrahlung emission will be polarized via Thomson scattering by

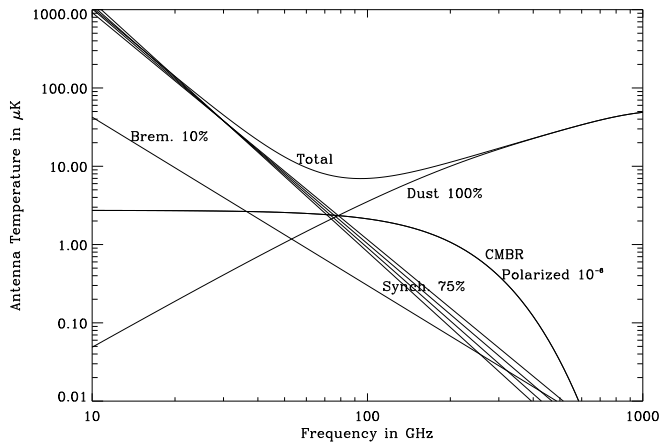


FIG. 4.—Polarized foreground spectra at millimeter wavelengths. Spectra of expected polarized radiation sources at high Galactic latitudes are shown for a  $7^\circ$  beam. A  $3 \mu\text{K}$  polarized CMB signal is shown, corresponding to 10% of the  $10^{-5}$  CMB anisotropy. At frequencies lower than 90 GHz, the polarization signal is dominated by Galactic synchrotron emission (up to 75% polarized, as shown). Galactic bremsstrahlung radiation is not polarized in direct emission but can be up to 10% polarized (as shown) after Thomson scattering. Galactic dust is shown conservatively, with 100% polarization.

the electrons in the H II region itself. The rescattered radiation will be polarized tangentially to the edges of the cloud at a maximum level of approximately 10% for an optically thick cloud. The locations and emissivities of Galactic H II regions are not well known, but Bennett et al. (1992) model the bremsstrahlung emission in the Galaxy by subtracting a synchrotron model from microwave sky maps. In any case, the polarization in the rescattered bremsstrahlung emission will be at least an order of magnitude smaller than the polarized synchrotron signal at frequencies greater than 10 GHz. We quote the result of Bennett et al. (1992) that

$$T_{\text{bremsstrahlung}} \propto \nu^{-2.15}, \quad (39)$$

with total intensity  $\sim 40 \mu\text{K}$  at 30 GHz (Kogut et al. 1996b; Bennett et al. 1992).

*Dust emission.*—The polarization level of interstellar dust is not well known. At low Galactic latitudes, thermal emission from dust particles dominates the near-infrared spectrum. Depending on the shape and the alignment of dust particles, emission from dust particles may be highly polarized (Wright 1987). Using the dust spectrum measured by the COBE FIRAS (Wright et al. 1991) normalized to the IRAS  $100 \mu\text{m}$  map, we find that high Galactic latitude dust emission is negligible below 80 GHz, even when it is assumed to be 100% polarized. We use the two-temperature dust model (Wright et al. 1991),

$$T_{\text{dust}} \propto \frac{c^2}{2\nu^2 k} \left( \frac{\nu}{900 \text{ GHz}} \right)^2 [B_\nu(20.4 \text{ K}) + 6.7B_\nu(4.77 \text{ K})]. \quad (40)$$

At high Galactic latitudes,  $T_{\text{dust}} \sim 10 \mu\text{K}$  at 200 GHz (Kogut et al. 1996b; Bennett et al. 1992).

*Extragalactic point sources.*—The dominant radiation mechanism for extragalactic radio sources is synchrotron emission (Sakia & Salter 1988). These sources have a net polarization of  $<20\%$ . Calculations made by Franceschini et al. (1989) of the temperature fluctuations in measurements of anisotropy of the CMB arising from unresolved, randomly distributed sources show that they contribute

negligibly at 30 GHz to a  $7^\circ$  anisotropy experiment. If the orientations of the polarization vectors of these sources are uncorrelated over  $7^\circ$  regions, we would also expect a negligible contribution to the signal observed by POLAR. We ignore the contribution of these sources in our foreground modeling.

*Atmospheric emission.*—The antenna temperature of the Earth's atmosphere between 10 and 60 GHz is dominated by an emission feature at  $\sim 22$  GHz caused by atmospheric water vapor and a series of emission lines at  $\sim 60$  GHz caused by molecular oxygen. In the absence of external fields, neither of these atmospheric components is known to emit polarized radiation in the frequency range of interest. However, Zeeman splitting of the energy levels of atmospheric molecules by the magnetic field of the Earth can produce polarized emission. The valence band of water is completely full and thus does not exhibit Zeeman splitting. However, the  $\text{O}_2$  molecule has a nonzero magnetic moment owing to its two unpaired valence electrons that interact with the Earth's magnetic field. We here discuss polarized emission from mesospheric oxygen and show that it is negligible in comparison with the expected polarized intensity of the CMB.

The Zeeman effect breaks the energy degeneracy of the two unpaired valence electrons of molecular oxygen. The total angular momentum quantum number of the oxygen molecule is  $j = 1$ , which implies that the oxygen molecule's rotational spectral lines are Zeeman split into  $2j + 1 = 3$  distinct lines. Dipole radiation selection rules for transitions between these levels permit transitions as long as the change in magnetic quantum number,  $m$ , is:  $\Delta m = 0, \pm 1$ . Transitions with  $\Delta m = +1$ , for example, correspond to the absorption of a right circularly polarized photon or the emission of a left circularly polarized photon. The absorption and emission properties depend, therefore, on both the frequency and polarization of the radiation. The frequency of each Zeeman split level is (Liebe 1981)

$$\nu_Z = \nu_0 + 2.803 \times 10^{-3} B \eta (\Delta m) \text{ GHz}, \quad (41)$$

where  $\nu_0$  is the unperturbed frequency,  $\eta$  is a shift factor with  $|\eta| \leq 1$ , and  $B$  is the magnitude of the Earth's magnetic field, typically 0.5 G throughout the mesosphere. The largest possible frequency shifts occur for  $\eta = \pm 1$ , which implies that the center frequencies for the polarized emission components will be confined to within 1.4 MHz of the unsplit center frequency. In principle, emission at these split frequencies could be up to 100% circularly polarized. Away from the center frequencies, the total intensity of emitted radiation decays with frequency as  $I \sim 1/(\nu - \nu_0)^2$  (P. W. Rosencranz 1994, private communication). For a small shift in frequency,  $\Delta\nu_0$ , away from the center frequency, the first order fractional change in emissivity can be shown to be

$$\frac{\Delta I}{I} = \frac{2\Delta\nu_0}{\nu - \nu_0}. \quad (42)$$

For a single Zeeman split component,  $\Delta I/I = 2\Delta\nu_{Z,\Delta m}/(\nu - \nu_Z)$ , where  $\Delta\nu_{Z,\Delta m} = \nu_Z - \nu_0 = 2.803 \times 10^{-3} B \eta (\Delta m)$  GHz, from equation (41). To obtain the total contribution to the emission of both polarization components, we must sum over left-handed and right-handed contributions,

$$\frac{\Delta I_{\text{tot}}}{I} = \sum_{\Delta m = \pm 1} \frac{2\Delta\nu_{Z,\Delta m}}{\nu - \nu_Z}. \quad (43)$$

However, for the shift factor in equation (41), we have  $\eta(\Delta m = +1) = -\eta(\Delta m = -1)$ , so the net effect on the emissivity is exactly canceled out by the two circularly polarized components (P. W. Rosencranz 1994, private communication). Any second order contributions to the emission scale as  $\sim 1/(\nu - \nu_z)^2$ , which implies a contribution of  $< 10^{-8}$  K for  $26 \leq \nu \leq 46$  GHz, i.e., the frequency band that POLAR will probe (B. P. Crill 1995, private communication). For these frequencies of observation, there is also a small Faraday rotation of the plane of polarization of the CMB. Rosencranz & Staelin (1988) show that the rotation of the plane of polarization will be less than  $\sim 10^{-2}$  deg for these frequencies. Therefore, both the polarized emission and the Faraday rotation of the atmosphere are negligible effects in the range of frequencies that POLAR will probe.

Of all the relevant foreground sources, only diffuse Galactic synchrotron radiation and dust are expected to appear at a level comparable to that of the anticipated polarized CMB signals (see Fig. 4). In the next section, we discuss techniques to remove spurious foreground sources using multifrequency observations.

## 5. FOREGROUND REMOVAL

Here, we estimate our ability to subtract foreground sources in the presence of atmospheric and instrumental noise. We apply two different approaches to foreground removal. In the first approach, we compute the anticipated error in our recovery of  $Q$  and  $U$  using an analytic technique developed by Dodelson (1997). In the second, Monte Carlo, approach, we create simulated data and use a least-squares fitting procedure to recover the underlying CMB  $Q$  and  $U$  parameters. We evaluate the quality of the fit by comparing the recovered and true CMB values. Results of these simulations are plotted in Figures 5 and 6.

### 5.1. Foreground Modeling

If there are several sources of polarized radiation at a given frequency in a given pixel, the Stokes parameter describing the total radiation is the sum of the Stokes parameters of each source. Following Dodelson (1997), we represent the total signal as

$$Q = \sum_{i=0}^3 q^i F^i + N_q \quad \text{and} \quad U = \sum_{i=0}^3 u^i F^i + N_u, \quad (44)$$

where the labels 0, 1, 2, and 3 represent the CMB, synchrotron radiation, bremsstrahlung, and dust-emission contributions to the total signal, respectively.  $Q$  and  $U$  are expressed in terms of antenna temperature. The thermodynamic temperatures of each signal source are  $q^i$  and  $u^i$ , and  $F^i$  are the spectral shapes of each source, following § 4.  $Q$  and  $U$  are written as vectors with dimensions equal to the number of observation frequencies. The components of  $Q$  and  $U$  are the Stokes parameters at that frequency; e.g.,  $Q = [Q(\nu_1), Q(\nu_2), \dots, Q(\nu_{N_{\text{obs}}})]$ . At frequency  $\nu$ ,

$$Q(\nu) = q^0 \frac{c^2}{2\nu^2} \frac{dB_\nu(T = 2.728 \text{ K})}{dT} + q^1 \nu^\beta + q^2 \nu^{-2.15} + q^3 \frac{c^2}{2\nu^2 k} \nu^2 [B_\nu(20.4 \text{ K}) + 6.7 B_\nu(4.77 \text{ K})] + N_q(\nu). \quad (45)$$

A similar equation holds for  $U$ .  $B_\nu(T)$  is a blackbody spectrum with thermodynamic temperature  $T$ .  $N_q$  and  $N_u$

each represent the combined contributions from instrument and atmospheric noise. For simplicity, we assume that the noise has the same Gaussian distribution for both  $Q$  and  $U$  and is the same for each frequency channel. Furthermore,  $\langle N \rangle = 0$  and  $\langle N^2 \rangle = \sigma^2$ .

The unknowns in the signal are the coefficients  $q^i$  and  $u^i$  and the synchrotron spectral index  $\beta$ . To simplify our notation, we write these intensity coefficients as vectors:  $\mathbf{q} = [q^0, q^1, q^2, q^3]$ . Note that  $q^0$  is the thermodynamic temperature corresponding to the  $Q$  Stokes parameter of the CMB and is frequency independent.

### 5.2. Error Analysis: Analytic Method

Our goal is to recover  $\mathbf{q}$  and  $\mathbf{u}$ , particularly  $q^0$  and  $u^0$ , from measured values of the  $Q$  and  $U$  Stokes parameters for each pixel at multiple observation frequencies. Given  $Q$  and  $U$ , it is convenient to consider  $I_{\text{pol}}$ , the linearly polarized intensity of the radiation  $I_{\text{pol}} = (Q^2 + U^2)^{1/2}$ , and the polar angle  $|\alpha| = \frac{1}{2} \tan^{-1}(U/Q)$ . Following Dodelson (1997), we wish to minimize the difference between the true CMB polarization signal and our best estimate of it. The fitting process is a  $\chi^2$  minimization for the linear unknowns that produces our best estimates for the intensity coefficients:

$$\mathbf{q}' = \kappa^{-1} \boldsymbol{\eta}_q \quad \text{and} \quad \mathbf{u}' = \kappa^{-1} \boldsymbol{\eta}_u,$$

where

$$\kappa^{ij} = \frac{\mathbf{F}^i \cdot \mathbf{F}^j}{\sigma^2}, \quad \eta_q^i = \frac{Q \cdot \mathbf{F}^i}{\sigma^2}, \quad \text{and} \quad \eta_u^i = \frac{U \cdot \mathbf{F}^i}{\sigma^2}.$$

Values of  $\mathbf{F}^i$  encode only the spectral shape (frequency dependence) of each foreground component. They are defined to be unit vectors such that  $\mathbf{F}^i \cdot \mathbf{F}^j = 1$  implies that  $\mathbf{F}^i$  and  $\mathbf{F}^j$  have the same frequency dependence. Note that the dimension of  $\mathbf{q}'$  and  $\mathbf{u}'$  may be different from that of  $\mathbf{q}$  and  $\mathbf{u}$  if we choose to restrict our attention to fewer foregrounds. The upper limit on the dimension of  $\mathbf{q}'$  and  $\mathbf{u}'$  is the number of frequencies of observation.

We define

$$i_{\text{pol}}^i = \sqrt{(q^i)^2 + (u^i)^2} \quad \text{and} \quad |\alpha^i| = \frac{1}{2} \tan^{-1} \left( \frac{u^i}{q^i} \right)$$

as the  $i$ th component's polarized intensity coefficient and polar angle. The errors in our analytic fitting process are

$$\text{error}(i_{\text{pol}}^i) = \sqrt{(\kappa^{-1})^{ii}} \equiv \sigma \epsilon^i \quad (46)$$

and

$$\text{error}(|\alpha^i|) = \frac{1}{2} \frac{\sqrt{(\kappa^{-1})^{ii}}}{i_{\text{pol}}^i} \equiv \frac{1}{2} \frac{\sigma \epsilon^i}{i_{\text{pol}}^i}. \quad (47)$$

We are interested in the recovery of the true CMB polarization intensity and orientation angle in the presence of the foregrounds. The error in the fitted CMB polarization intensity coefficient,  $\text{error}(i_{\text{pol}}^0)$ , is found from equation (46) to be the standard deviation of the system (instrumental + atmospheric) noise multiplied by a factor,  $\epsilon^0$ , which depends only on the frequencies of observation and the choice of foregrounds which are fitted. It can be normalized such that its minimum value (i.e., with no foregrounds or system noise) is 1.0. The normalized parameter, known as the ‘‘foreground degradation factor’’ (‘‘FDF’’;

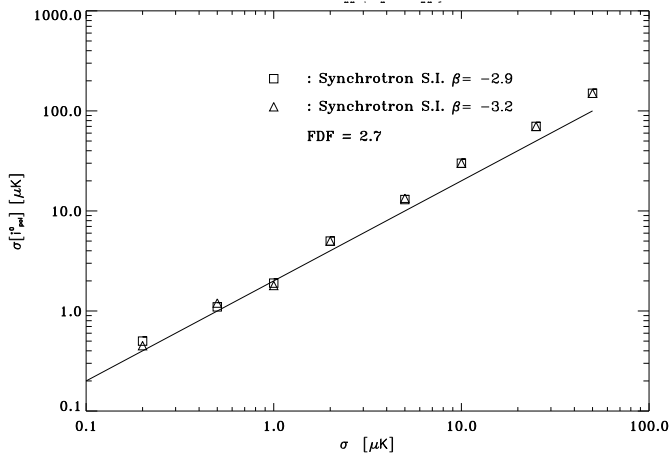


FIG. 5.—Recovery of CMB polarization intensity coefficient vs. system noise. This plot shows the results of the simulations described in § 5. The vertical axis is the error in the recovered CMB polarization intensity for a single pixel in  $\mu\text{K}$ . The plotted symbols are the Monte Carlo simulation results for two different values of the synchrotron spectral index; the solid line is the analytic result for the foreground degradation factor. The analytic and Monte Carlo results agree extremely well. This figure demonstrates the feasibility of detecting a CMB signal polarized at the  $\sim 1\text{--}3\ \mu\text{K}$  level using a two-frequency configuration. For such a detection, the system noise, defined over the entire observing time, must be below  $1\ \mu\text{K}$ .

Dodelson 1997), is

$$\text{FDF} = \epsilon^0 \sqrt{F^0 \cdot F^0}.$$

An optimized experiment will minimize not only the system noise  $\sigma$  but also the FDF. Another contribution to the analytic error defined by Dodelson (1997) is the error arising from the uncertainty in the spectral shape functions,  $F^i$ , of the foregrounds, which vary with position on the sky. The situation is now more complicated because we must compute these contributions separately for both  $Q$  and  $U$ . This error, called “ $\sigma_{\text{shape}}$ ” by Dodelson (1995), is negligible

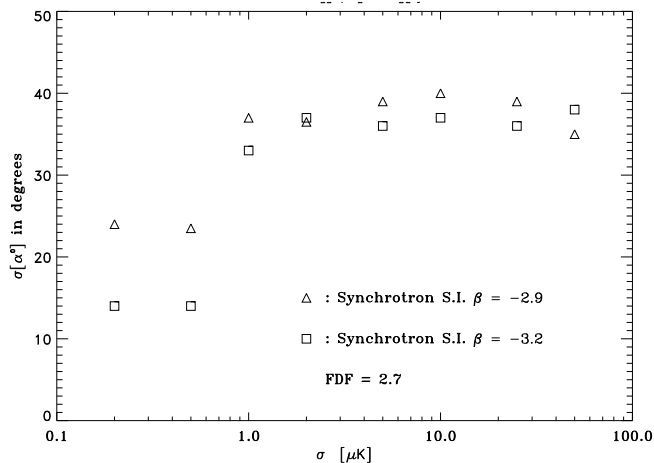


FIG. 6.—Recovery of polarization orientation angle vs. system noise. This plot shows the results of the simulation described in § 5. The vertical axis is the error in degrees in the recovered CMB polar angle for a single pixel. The plotted symbols are the Monte Carlo simulation results for two different values of the synchrotron spectral index. As in the polarized intensity recovery Fig. 5, accuracy in the recovery of the CMB polar angle depends primarily on the system noise, which is defined over the entire observing time. Recovery of the CMB polar angle with errors less than  $30^\circ$  is only possible if the system noise is lower than  $1\ \mu\text{K}$ .

for our most important foreground, synchrotron radiation, even though we know  $\beta$  to only 10%.

### 5.3. Error Analysis: Monte Carlo Method

To corroborate the results of the analytic error calculation, we perform a more explicit foreground removal simulation. The approach is similar to that of Brandt et al. (1994). First, we choose a particular set of observing frequencies. Using equation (45), at each pixel we create simulated signals for each frequency using foreground levels typical of high Galactic latitude regions. While the foreground temperatures are fairly well known, the polarization levels are not, and we choose the most conservative estimates: 75% for synchrotron radiation, 10% for bremsstrahlung radiation, and 100% for dust. The CMB signal is chosen nominally at 10% of the anisotropy level ( $\sim 3\ \mu\text{K}$ ), but the results of the simulation are independent of the exact value. For each of these signals, we keep the true intensity,  $\equiv i_{\text{pol}}^i$ , fixed but allow the orientation,  $\equiv \alpha^i$ , to vary randomly. Noise is chosen from a Gaussian distribution with standard deviation  $\sigma$  in each frequency channel and added as in equation (45). We then perform a least-squares fit to a particular signal and foreground model and determine our best-fit values for the recovered CMB intensity  $i_{\text{pol}}^0$  and orientation angle  $\alpha^0$ . We repeat this process 200 times, generating new values for the system noise and for  $\alpha^i$  each time. Finally, we compute the rms of the difference between the 200 input CMB coefficients,  $i_{\text{pol}}^0$ , and the corresponding best-fit CMB values,  $i_{\text{pol}}^0$ . A similar procedure is conducted for the true CMB polarization orientation angle,  $\alpha^0$ , and the recovered angle,  $\alpha^0$ . In this process, we average over many different relative orientations of the polarized foreground vectors.

Typically the number of foregrounds (e.g., four) simulated is greater than the number of frequency channels (e.g., two or three), so we can fit for only some of the signals (e.g., the CMB and one or two foregrounds). As shown below, for a judicious choice of the observation frequency channels, the neglected foregrounds will not contribute significantly to the error in the recovery of the CMB signal.

The primary unknown that is not determined by this analysis is the synchrotron spectral index, which varies with sky position. We estimate an uncertainty in the synchrotron spectral index by using a range of values for the fitting function  $F^1(\nu) = \nu^\beta$ . We evaluate  $F^1(\nu)$  for three values of the spectral index,  $\beta = -2.9, -3.05,$  and  $-3.2$ .

### 5.4. Results of Error Analysis

Here we concentrate on a system noise range of  $0.2\text{--}50\ \mu\text{K}$  (after a long integration on each pixel) and show the results of a two-channel configuration observing at 30 and 40 GHz, which is appropriate for POLAR. Here, the only foreground considered is synchrotron radiation, and we find that the degradation to our experimental sensitivity is  $\text{FDF} = 2.7$ . Other frequency channel configurations show, very generally, that in order to fit for an extra foreground source (e.g., dust emission) without a severe increase in the FDF, one must observe more than three frequency channels.

The plots of polarized intensity coefficient error versus system noise demonstrate that the quality of the recovery is fairly insensitive to the value of the input synchrotron spectral index. The Monte Carlo results are plotted as points, and the analytic result is plotted as a line. The excellent

agreement of our analytic and Monte Carlo results confirms the idea that a successful observation should have a small  $\epsilon^0$  or, equivalently, a low FDF.

For CMB polar angle recovery, the plotted symbols represent Monte Carlo simulations at the two extreme values of the synchrotron spectral index. Generally, the polar angle is more difficult to determine than the total linear polarized intensity, even at very low values of system noise. However, frequency configurations that yield an accurate recovery of the total polarized intensity will often give a more accurate recovery of the polar angle as well.

From our analysis and simulation of CMB polarization, we conclude that for a dual-frequency experiment observing frequencies below 60 GHz, the most important challenge is to reduce the system noise. The contribution of the system noise is far more important than that of combining bremsstrahlung and synchrotron radiation in the fitting process or of reducing the uncertainty in the synchrotron spectral index used to fit the data. We conclude that an experiment of the 30–40 GHz type with system noise lower than  $1 \mu\text{K}$  is capable of discriminating a  $\sim 1\text{--}3 \mu\text{K}$  CMB polarization signal from polarized Galactic synchrotron radiation.

## 6. OBSERVATION STRATEGY

Constraints on, or detection of, the polarization of the CMB and its associated power spectrum depend greatly on the amount of sky coverage of the observation and the sensitivity of the radiometer. Sensitivity considerations are common to all CMB observations: time limitations restrict signal integration and constrain the amount of sky coverage. We must reach a compromise between the integration time required to achieve the desired signal-to-noise ratio while also sampling a representative distribution of celestial regions. We now discuss our observing strategy in the context of the achievable level of sensitivity of POLAR.

### 6.1. Sky Coverage

The trade-off between the signal-to-noise ratio (S/N) per pixel and the total number of pixels arises frequently in designing CMB observing strategies. The ultimate goal is to discriminate between two hypotheses,  $H_0$  and  $H_{\text{pol}}$ , which are the null hypothesis of an unpolarized CMB and the hypothesis that the CMB is polarized at a particular level. This discrimination is quantified by the confidence level and power of the measurement. POLAR seeks to make a primary detection, namely, a detection of a signal for which no prior detections have been made. There are four possible outcomes: the first two are correct detections of either  $H_0$  or  $H_{\text{pol}}$ . The other two outcomes are erroneous detections, a false positive or a false negative detection. Maximizing the confidence level minimizes the probability of a false detection, while maximizing the power minimizes the probability of making a false negative detection. Power quantifies the ability of an experiment to distinguish between competing hypotheses and confidence quantifies the certainty of the detection. Traditionally, most CMB experiments have quoted only confidence intervals. Keating & Polnarev (1998) argue that the confidence level should be equal to the discriminating power for a primary detection.

For a fixed total amount of observing time, we wish to find the number of pixels that maximizes the confidence level and the power of the experiment. We estimate the polarized CMB intensity from models described above.

While our S/N per pixel is  $< 1$  (see § 3), we expect that our signal-to-noise ratio defined over the total observation time, denoted by  $R$ , will be  $R \sim 1$ . For  $R = 1$ , it is shown that the optimum number of pixels is  $\sim 10$ , with a very weak dependence of the optimum on  $N$ . In order to minimize the susceptibility to certain systematic effects, as discussed above, POLAR observes a constant declination that corresponds to the zenith. The number of independent pixels that will be observed is  $N = 360^\circ \cos \theta_{\text{lat}} / \Theta_A$ , where  $\theta_{\text{lat}}$  is the latitude of Madison, Wisconsin, and  $\Theta_A$  is the antenna full width at half-maximum, FWHM. We find  $N \sim 36$ , though we are free to pixelize our data into bins that are smaller than this, for instance, at the “Gaussian width” of our antenna,  $\sigma_B = \text{FWHM} / [2(\ln 2)^{1/2}]$ . Observing fewer pixels would increase the S/N per pixel but would either require tracking individual pixels over large angles on the sky or tilting the radiometer toward the north celestial pole. Either approach would undoubtedly introduce gravitationally modulated systematic effects into our data. Additionally, with  $N \sim 36$ , we will have good coverage of the Galaxy, which should allow for both the removal of foregrounds and a comparison with previous Galactic polarization surveys (e.g., Brouw & Spoelstra 1976). For  $N = 36$  and  $R = 1$ , POLAR can expect to make a detection at the  $\sim 55\%$  level of confidence and power for a CMB that is polarized at  $\sim 1 \mu\text{K}$ . Of course, it is still possible to quote results with confidence arbitrarily close to 100%, but this would be at the expense of ability to reject the null hypothesis (i.e., low power). In the context of a primary detection, requiring equal levels of confidence and power seems the most reasonable compromise.

### 6.2. Sensitivity to the Power Spectrum

The observation’s sensitivity to CMB fluctuations is quantified by its window function,  $W_\ell$ . The observed two-point correlation function is related to the power spectrum and window function as follows:

$$\langle Q(\hat{n}_1)Q(\hat{n}_2) + U(\hat{n}_1)U(\hat{n}_2) \rangle = \frac{1}{4\pi} \sum_{\ell=0}^{\infty} (2\ell + 1) \times C_\ell^{\text{II}} W_\ell^\theta \times P_\ell(\cos \theta), \quad (48)$$

where, for example,  $Q(\hat{n})$  is the Stokes parameter measured for a pixel located in the direction  $\hat{n}$ .  $C_\ell^{\text{II}}$  is the power spectrum describing the degree of polarization on angular scales characterized by  $\ell$ ,  $W_\ell^\theta$  is the window function of this observing scheme, and  $\cos(\theta) = \hat{n}_1 \cdot \hat{n}_2$  is the separation between pixels in this observing scheme.

The analysis differs from that of most anisotropy experiments in several respects. The primary difference is that the observations are total-power in nature, rather than differential. The window functions for this experiment will reflect the fact that there is no “chopping” of the beam in sky position inherent in the observation. Single pixels will be formed by binning the acquired data, and differencing between pixels can be performed during analysis of the data, not during acquisition. This approach avoids systematic effects that can arise from mechanical chopping mechanisms. Data from POLAR will be analyzed using a variety of synthesized window functions, each sensitive to a different angular scale. In this respect, the analysis will be similar to that of the Saskatoon Big Plate observations (Netterfield et al. 1995; Wollack et al. 1997).

Window functions for observations with less than full-sky coverage are specified by three functions, the beam profile function, the beam position function, and the weighting or “lock-in” function (White & Srednicki 1995). The beam profile function  $G(\theta, \theta_i, \sigma_B)$ , where  $\sigma_B$  is the beamwidth, quantifies the directional response of the antenna, which is assumed to be Gaussian.  $G(\theta, \theta_i, \sigma_B)$  effectively samples all angular scales larger than, approximately, the angular size of the beam. The angular coordinates of the center of the beam are specified by the beam position function  $\theta_i$ , and the lock-in function  $w_i^\alpha$  is the weighting of each of the  $N$  binned pixels indexed by  $i$  for the scan strategy denoted by  $\alpha$ . We have  $G(\theta, \theta_i, \sigma_B) = 1/(2\pi\sigma_B^2) \exp[-(\theta - \theta_i)^2/2\sigma_B^2]$ , where  $\sigma_B = \text{FWHM}/[2(2\ln 2)^{1/2}] = 0.052$ .

Following White & Srednicki (1995), the window functions are

$$W_\ell^{\alpha\beta} \equiv \int d\hat{x}_1 \int d\hat{x}_2 H^\alpha(\hat{x}_1) H^\beta(\hat{x}_2) P_\ell(\hat{x}_1 \cdot \hat{x}_2), \quad (49)$$

where  $P_\ell$  are the Legendre polynomials and  $H^\alpha(\hat{x}) = \sum_i w_i^\alpha G(\theta, \theta_i, \sigma_B)$  quantifies the response of the antenna (for a differencing strategy indexed by  $\alpha$ ) when pointed in the direction of  $\hat{x}$ . For a Gaussian beam,  $H^\alpha(\hat{x}) = \sum_i w_i^\alpha 1/(2\pi\sigma_B^2) \exp[-(\theta - \theta_i)^2/2\sigma_B^2]$ .

By varying the weight function, we will obtain window functions “tuned” to sample specific multipole-space regions. For example,  $w_i^\alpha = (-1)^{i+1}$  differences pairs of nearest neighbor pixels. Pairs of pixels will be separated by a constant angle for each differencing strategy indexed by  $\alpha$ , which runs from 1 to 18, corresponding to the  $N/2$  distinct 2 pixel difference window functions of POLAR. The number of unique 2 pixel combinations,  $k$ , is given by  $k = N!/[N(N-1)]$ , where  $N$  is the number of binned pixels and  $m$  is the number of beams that are differenced. For  $N = 36$  pixels differenced pairwise ( $m = 2$ ),  $k = 630$ . We note that the total-power nature of POLAR, as well as the insensitivity of our experiment to atmospheric emission and thermal gradients, will allow us to perform 2 pixel differencing, in contrast to the majority of ground-based CMB anisotropy observations, which typically difference 3 or more pixels.

To estimate the rms polarization for the  $\text{FWHM} = 7^\circ$  polarimeter with 36 pixels, we have calculated the single-pixel window function of POLAR,  $W_\ell^{\alpha\alpha}$ . This contains only the diagonal elements of the window-function matrix from equation (49). This quantity will allow us to determine the relationship between the measured pixels and the underlying spectrum that is responsible for a particular realization on the sky. The polarization two-point covariance matrix (at zero lag) for a particular theoretical model is given by

$$C_{\Pi}^{\alpha\beta} = \frac{1}{4\pi} \sum_\ell (2\ell + 1) C_\ell^\Pi W_\ell^{\alpha\beta}. \quad (50)$$

To compute the theoretical rms amplitude, we extract the square root of the diagonal elements of  $C_{\Pi}^{\alpha\beta}$  and obtain

$$\Pi_{\text{rms}}^\alpha = \sqrt{\frac{1}{4\pi} \sum_\ell (2\ell + 1) C_\ell^\Pi W_\ell^{\alpha\alpha}},$$

where  $C_\ell^\Pi$  have been introduced in § 2. We show this window function in Figure 2. Of course, the off-diagonal components of the window-function matrix will contain additional information about cross-correlation between

pixels, as opposed to  $W_\ell^{\alpha\alpha}$ , which is the auto-correlation. The off-diagonal window-function matrix elements will increase the effective signal-to-noise ratio of the experiment as a whole and can be “tuned” to sample-specific  $\ell$ -space regions, up to the cutoff  $\ell$  of the antenna, similarly to the analysis of (Netterfield et al. 1995). For anisotropy experiments, it is conventional also to quote the band power, which is independent of the details of the experiment. This approach facilitates comparisons between experiments and contains information equivalent to that of the rms amplitude.

### 6.3. Estimated Signal Level and Uncertainty

The primary goal of POLAR is to measure the polarization of the CMB. We have shown in § 2 that the level of polarization is extremely sensitive to the ionization history of the universe, both before and after recombination. We expect, then, that the observed polarization signal will depend critically on the optical depth  $\tau$  for photons back to the last scattering surface. A preliminary estimate of the effect of reionization can be obtained by computing the expected rms polarization and associated experimental uncertainty for models of a reionized universe. We will now compute the effect of reionization on the power spectrum and demonstrate that the characteristic signature of an early reionization is, in principle, detectable by POLAR.

Figure 2 displays  $C_\ell^\Pi$  for the power spectrum computed using CMBFAST (Seljak & Zaldarriaga 1996) for various totally reionized (ionized fraction  $x = 1$ ) scenarios, parameterized by the redshift of reionization  $z_{\text{ri}}$ . In Figure 7, we plot the expected rms polarization versus  $z_{\text{ri}}$  for  $0 < z_{\text{ri}} < 105$ , along with the statistical  $1\sigma$  uncertainties we expect based on our NET and observation time. The underlying power spectrum is a generic CDM model with  $\Omega = 1$ ,  $\Omega_B = 0.05$ ,  $h = 0.65$ ,  $\Lambda = 0$ , and pure scalar perturbations. The inclusion of a tensor component should enhance the large angular scale polarization (Crittenden et al. 1993; Crittenden, Coulson, & Turok 1995), so this figure underestimates the rms polarization predicted by some cosmological models. This figure suggests that POLAR could begin to detect polarization of the CMB at the  $1\sigma$  level

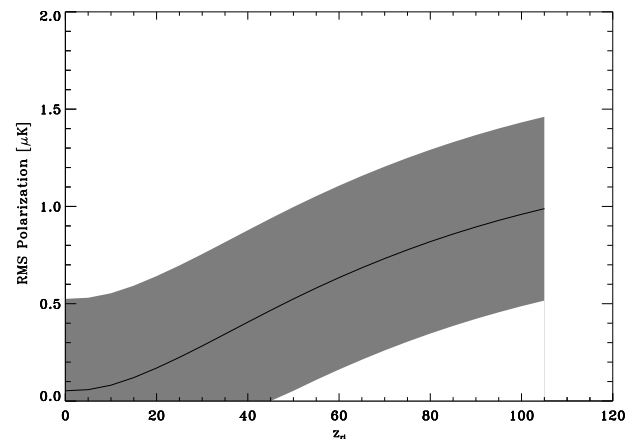


FIG. 7.—Expected rms polarization in reionized universes. The solid line is the magnitude of the rms CMB polarization as a function of redshift of reionization. All reionization scenarios assume total ionization ( $x = 1$ ), except for  $z_{\text{ri}} = 0$ , which represents no reionization. The gray band represents the  $1\sigma$  experimental uncertainty for POLAR, observing 36 pixels for a total time of  $1 \times 10^7$  s with  $\text{NET} = 460 \mu\text{K s}^{1/2}$ , after simulated foreground subtraction.

if the universe became completely reionized at a redshift  $z_{\text{ri}} > 45$ .

## 7. RELATED TOPICS

Although no detections of the polarization have been made, we can glean information about CMB polarization from anisotropy detections. In principle, these detections can be utilized to refine a polarization observing strategy. Here, we briefly discuss the possibility of designing a polarization observing strategy, utilizing information from a well-sampled anisotropy map.

Anisotropy and polarization are invariably spatially correlated with one another, and additional cosmological information may be obtained by studying polarization-polarization and polarization-anisotropy correlation functions. Correlation provides the only link between previous detections (of anisotropy) and the proposed measurements discussed in this article. CMB polarization can be decomposed into two components, one that is spatially correlated with the temperature anisotropy and another, larger, component that is uncorrelated. Ng & Ng (1996) and Crittenden et al. (1995) demonstrate that, given a high-resolution CMB temperature map, it would be possible to identify celestial regions that are statistically more likely to possess higher levels of the correlated polarization component. As shown in Coulson, Crittenden, & Turok (1994), the uncorrelated polarization component dominates the correlated component by a factor of at least 3.

For polarization experiments limited by detector noise, it can be advantageous to search for polarization-anisotropy  $\langle QT \rangle$  correlation in addition to polarization-polarization  $\langle QQ \rangle$  cross-correlation. If the noise in the temperature anisotropy map is negligible in comparison to the noise of the polarization measurement  $\sigma$ , the error in  $\langle QT \rangle$  will be linear in  $\sigma$ , while the variance in the polarization cross-correlation function grows as  $\sigma^2$ . In this limit, it becomes advantageous to search for correlation.

Power spectrum generation programs such as CMBFAST compute  $\langle QT \rangle$ , along with the anisotropy and polarization spectra. This allows one to predict the distribution of polarization that is correlated with the anisotropy given a well-sampled anisotropy map. Finally, Crittenden et al. (1995) describe potentially observable distributions of correlated polarization vectors on the sky that result from the velocity field of the photon-electron plasma and the type of metric perturbation that generates the anisotropy. If the angular resolution and experimental sensitivity of measurements improve by several orders of magnitude over the current levels, these patterns could prove to be direct observables of the microphysical properties of the photon-baryon fluid at the moment of decoupling.

We also briefly discuss an effect that is peculiar to CMB polarization measurements: Faraday depolarization of the CMB by primordial magnetic fields. Faraday depolarization causes the plane of CMB polarization to rotate dif-

ferentially because of a residual primordial magnetic field that may have existed during the epoch of recombination (Basko & Polnarev 1980). The effect is akin to optical dichroism, familiar from the polarization of visible light. The net depolarization is frequency dependent, as the rotation of the plane of polarization of individual frequency components scales as  $\sim 1/\nu^2$ . This effect is expected to be nonnegligible below 30 GHz for reasonable values of the primordial magnetic field (Harari, Hayward, & Zaldarriaga 1997; Kosowsky & Loeb 1996). Detection of this effect is unlikely until the polarization of the CMB has been detected over a large frequency bandwidth and with high angular resolution. Neither of the above mentioned phenomena are immediately relevant for polarization observations, but both are nonetheless quite intriguing.

## 8. CONCLUSION

We have demonstrated that detection of the polarization of the CMB is difficult but technologically feasible. A detection would permit discrimination between heretofore degenerate theoretical predictions. Polarization of the CMB has a unique signature in both real and Fourier space, as well as distinct spectral characteristics. A detection of polarization in conjunction with the current detections of CMB anisotropy could be the best available probe of the ionization history of the pregalactic medium. This epoch of cosmic evolution is of great interest, and supplemental information from polarization detection could greatly advance our knowledge of the formation of structure in the early universe. The current generation of anisotropy measurements are sufficiently refined that the fundamental parameters of classical cosmology are beginning to be determined. Detection of polarization of the CMB also promises numerous dividends throughout cosmology, and one readily observes that the status of polarization observations today is reminiscent of the status of anisotropy measurements a decade ago.

The authors are indebted to many people who have worked on the planning and development of this measurement. Khurram Farooqui and Grant Wilson designed an early version of the instrument and observing scheme. Brendan Crill tested the polarimeter and calculated the atmospheric emission. Victor Derderian designed the rotation platform of the instrument. Melvin Phua and Nathan Stebor helped to diagnose systematic effects. Dave Wilkinson made key suggestions regarding the design of the correlation radiometer. Jeff Peterson reviewed the manuscript and made helpful suggestions. Conversations with Robert Brandenberger, Josh Gundersen, Ka Lok Ng, Lucio Piccirillo, Uros Seljak, and Matias Zaldarriaga have refined the focus of the project. This work is supported by NSF grant AST 93-18785, a Ford Motor Company University Research Grant, a NASA GSRP Fellowship for B. K., and a UTRA grant from Brown University for J. S.

## REFERENCES

- Basko, M. M., & Polnarev, A. G. 1980, MNRAS, 191, 207  
 Bennett, C. L., Hinshaw, G., Banday, A., Kogut, A., Wright, E. L., Lowenstein, K., & Cheng, E. S. 1993, ApJ, 414, L77  
 Bennett, C. L., et al. 1992, ApJ, 396, L7  
 ———. 1996, ApJ, 464, L1  
 Bond, J., & Efstathiou, G. 1984, ApJ, 285, L45  
 ———. 1987, MNRAS, 226, 655  
 Brandt, W., Lawrence, C. R., Readhead, A. C. S., Pakianathan, J. W., & Fiola, T. M. 1994, ApJ, 424, 1  
 Brouw, W. N., & Spoelstra, T. A. 1976, A&AS, 26, 129  
 Caderni, N. 1978, Phys. Rev. D, 17, 1908  
 Chandrasekhar, S. 1960, Radiative Transfer (New York: Dover)  
 Cortiglioni, S., & Spoelstra, T. 1995, A&A, 302, 1  
 Coulson, D., Crittenden, R. G., & Turok, N. G. 1994, Phys. Rev. Lett., 73, 2390  
 Crittenden, R., Coulson, D., & Turok, N. 1995, Phys. Rev. D, 52, r5402  
 Crittenden, R. G., Davis, R., & Steinhardt, P. 1993, ApJ, 417, L13  
 Dodelson, S. 1997, ApJ, 482, 577

- Durrer, R. 1994, *Fundam. Cosmic Phys.*, 15, 209
- Fixsen, D., Cheng, E. S., Gales, J. M., Mather, J. C., Shafer, R. A., & Wright, E. L. 1996, *ApJ*, 473, 576
- Franceschini, A., Toffolatti, L., Danese, L., & De Zotti, G. 1989, *ApJ*, 344, 35
- Frewin, R., Polnarev, A., & Coles, P. 1994, *MNRAS*, 266, L21
- Fujimoto, K. 1964, *IEEE-MTT*, MTT, 203
- Gooding, A. K., et al. 1991, *ApJ*, 372, 15
- Gunn, J. E., & Peterson, B. A. 1965, *ApJ*, 142, 1633
- Harari, D. D., Hayward, J. D., & Zaldarriaga, M. 1996, *Phys. Rev. D*, 55, 1841
- Harari, D. D., & Zaldarriaga, M. 1993, *Phys. Lett. B*, 319, 96
- Hu, W. 1995, Ph.D. thesis, Univ. California, Berkeley
- Janssen, M. A., et al. 1979, *IEEE Trans. Antennas Propagation Soc.*, AP-27(4), 551
- Kamionkowski, M., et al. 1998, in preparation
- Keating, B., & Polnarev, A. 1998, *ApJ*, submitted
- Kogut, A., et al. 1996a, *ApJ*, 470, 653
- Kogut, A., Banday, A. J., Bennett, C. L., Gorski, K. M., Reach, W. T., & Hinshaw, G. 1996b, *ApJ*, 460, 1
- Kosowsky, A. 1996, *Ann. Phys.*, 246, 49
- Kosowsky, A., & Loeb, A. 1996, *ApJ*, 469, 1
- Krauss, J. 1982, *Radio Astronomy* (New York: McGraw-Hill)
- Liebe, H. 1981, *Radio Sci.*, 16, 1183
- Lubin, P. 1980, Ph.D. thesis, Univ. California, Berkeley
- Lubin, P., Melese, P., & Smoot, G. 1983, *ApJ*, 273, L51
- Lubin, P., & Smoot, G. 1981, *ApJ*, 245, 1
- Nanos, G. 1979, *ApJ*, 232, 341
- Nasel'skii, P., & Polnarev, A. 1987, *Astrofizika*, 26, 327
- Negroponete, J., & Silk, J. 1980, *Phys. Rev. Lett.*, 44, 1433
- Netterfield, C. B., Jarosik, N., Page, L., Wilkinson, D., & Wollack, E. 1995, *ApJ*, 445, L69
- Ng, K. L., & Ng, K. W. 1995, *Phys. Rev. D*, 51, 364
- . 1996, *ApJ*, 456, 413
- Ozernoi, L. M., & Chernomordik, V. V. 1975, *Soviet Astron.*, 20, 260
- Partridge, R., et al. 1988, *Nature*, 331, 146
- Peebles, P. 1993, *Principles of Physical Cosmology* (Princeton: Princeton Univ. Press)
- Penzias, A., & Wilson, R. 1965, *ApJ*, 142, 419
- Polnarev, A. G. 1985, *AZh*, 62, 1041
- Pospiszalski, M. 1992, *IEEE-MTT-S Digest*, 1369
- . 1995, *IEEE-MTT-S Digest*, 1121
- Rees, M. J. 1968, *ApJ*, 153, L1
- Rohlfs, K. 1990, *Tools of Radio Astronomy* (New York: Springer)
- Rosencranz, P. W., & Staelin, D. H. 1988, *Radio Sci.*, 25, 721
- Rybicki, G. B., & Lightman, A. 1979, *Radiative Processes in Astrophysics* (New York: Wiley)
- Sachs, R. K., & Wolfe, A. M. 1967, *ApJ*, 147, 73
- Sakia, D., & Salter, C. 1988, *ARA&A*, 26, 93
- Scott, D., Silk, J., & White, W. 1995, *Science*, 268, 829
- Seljak, U., & Zaldarriaga, M. 1996, *ApJ*, 469, 437
- . 1998, in preparation
- Tegmark, M., & Silk, J. 1993, in *Present and Future of the CMB*, ed. J. L. Sanz, E. Martinez-Gonzalez, & L. Cayon (Berlin: Springer)
- Tolman, B. W. 1985, *ApJ*, 290, 1
- White, M., & Srednicki, M. 1995, *ApJ*, 443, 6
- Wilkinson, D. T. 1995, in *Particle Physics and Cosmology*, ed. A. Astbury (Singapore: World Scientific), 110
- Wollack, E. J., Devlin, M. J., Jarosik, N., Netterfield, C. B., Page, L., & Wilkinson, D. 1997, *ApJ*, 476, 440
- Wollack, E. J., Jarosik, N. C., Netterfield, C. B., Page, L. A., & Wilkinson, D. 1993, *ApJ*, 419, L49
- Wright, E. L. 1987, *ApJ*, 320, 818
- Wright, E. L., et al. 1991, *ApJ*, 381, 200
- Zaldarriaga, M. 1997, *Phys. Rev. D*, 55, 1822
- Zaldarriaga, M., & Harari, D. 1995, *Phys. Rev. D*, 52, 3276
- Zaldarriaga, M., & Seljak, U. 1997, *Phys. Rev. D*, 55, 1830